Supplementary Information

Supplementary texts S1, S1.1-1.3

Figures S1.1-1.4

Table S1.1

Supplementary texts S2.1-2.3

Supplementary texts S3.1-3.2

Figures S3.1-3.6

Tables S3.1-3.8

Supplementary texts S4.1-4.5

Figures S4.1-4.8

Tables S4.1-4.2

Supplementary Text S1 Geomorphology analysis

S.1. Seismic survey

The high resolution seismic geophysical dataset was acquired between October 2008 and March 2009 as two separate surveys by Gardline Surveys Limited as part of the ALSF funded Humber REC survey (Tappin et al. 2011). The data was obtained by the Gardline Vessel *Vigilant*, which was equipped with a surface-towed boomer system consisting of an Applied Acoustics 300 Plate powered by an Applied Acoustics CSP 1500 Pulse Generator. The receiver consisted of a 12-element single channel hydrophone eel recorded with a Gardline 2012. Digital data logging and initial processing was accomplished using an Octopus 760 geophysical acquisition package (CodaOctopus). During acquisition a swell filter was applied to the data when necessary to correct for the effects of sea swell. The system was operated at a power level of 300 joules with a 350-millisecond fire rate. This equipment setup was used on all profiles with useful data generally recovered to a depth in excess of 25 metres below seabed. The data was initially inspected, and processing accomplished using both SonarMap (Chesapeake Ltd) and GeoSurvey (Coda Ltd) with further processing utilising IHS Kingdom. A number of post-acquisition processing steps were applied to the data which included bandpass filtering, time varied gain and running-sum amplitude gain correction. Sub-surface layers were first-break picked from refracted seismic signals where evident above background noise.

The seismic reflection later associated with the Tsunami deposit was characterized by a negative amplitude of response from -18,000 to -26,000 as well as a sharp phase transition within the wavelet of response from -165 to +171 degrees. This signal was a distinct response within the seismic line and occurred broadly along the same time interval, between 0.035 and 0.037 seconds, indicating a distinct stratum. The signal was not repeated

in any of the deeper parts of the seismic line, nor observed in seismic lines outside of the basin surrounding core ELF001A (Figure S1.1). This signal was therefore deemed to be a unique character to this area of the survey. Because of the unique nature of the signal, coring this unit (ELF001A) was undertaken in 2016 to determine the origin of this reflection (Figure S1.2), whereupon subsequent lithological, environmental proxy and dating analyses established the presence of a tsunami deposit (see following methods). Once the reflection had been identified as a tsunami deposit within the core, the seismic signal was re-examined and the correlation between reflector depth against the deposit depth was verified.

When the seismic line was examined, similar responses were noted in patches within three distinct geographic areas within the basin, one 1.96km along the line to the East, a central section 1.40km along the line, where ELF001A was recovered, and a smaller western section 540m along the line (Figure S1.2A.). After the recovery of ELF001A, the discontinuous nature of this reflector was interpreted to relate to post tsunami erosion, occurring during the inundation and submergence of this area. Using this knowledge, cores ELF003 and ELF0059 were identified as candidates to also include traces of the tsunami deposit (Figure S1.1). These patches of similar seismic response were recorded during the re-examination of the data to assist interpretation and guide future survey in these areas.

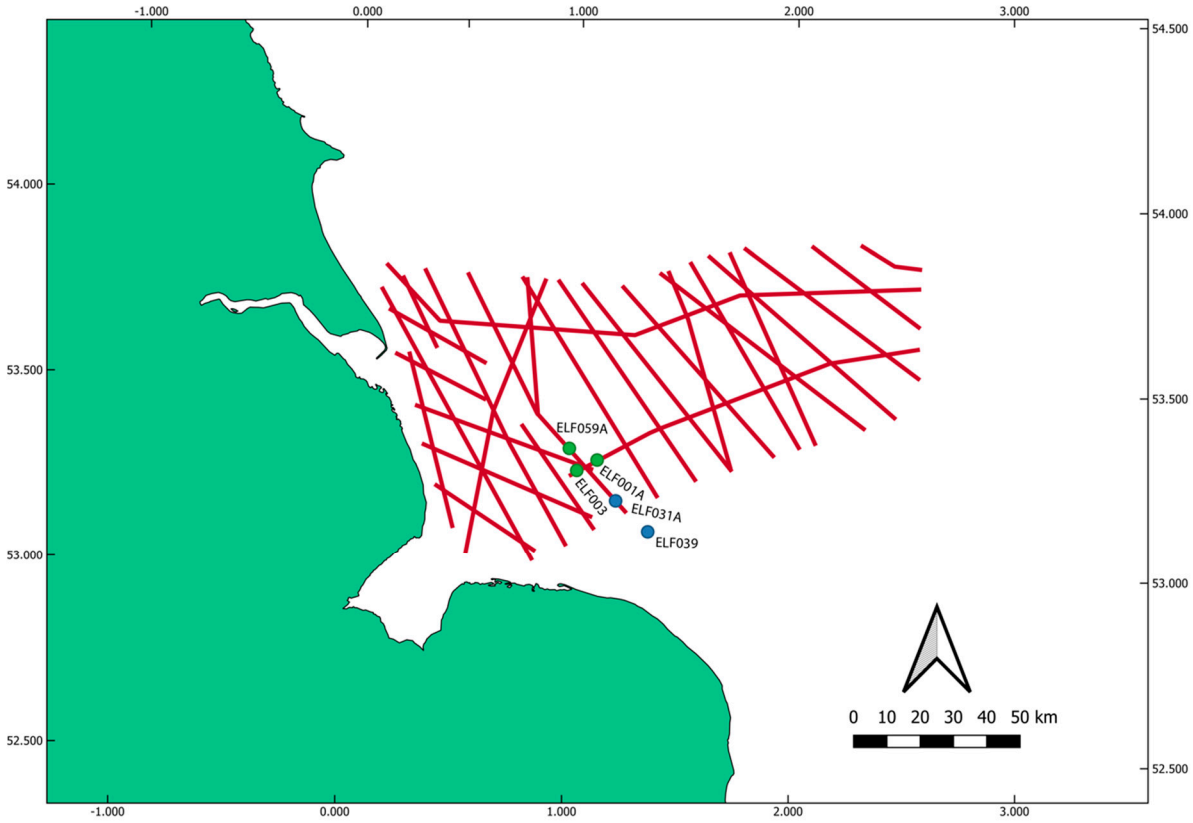

Figure S1.1 Location of the 2D seismic survey lines and tsunami associated core locations. Cores identified with Tsunami material within the basin are marked green, whilst those identified to be associated with the drainage via the southern river are marked blue

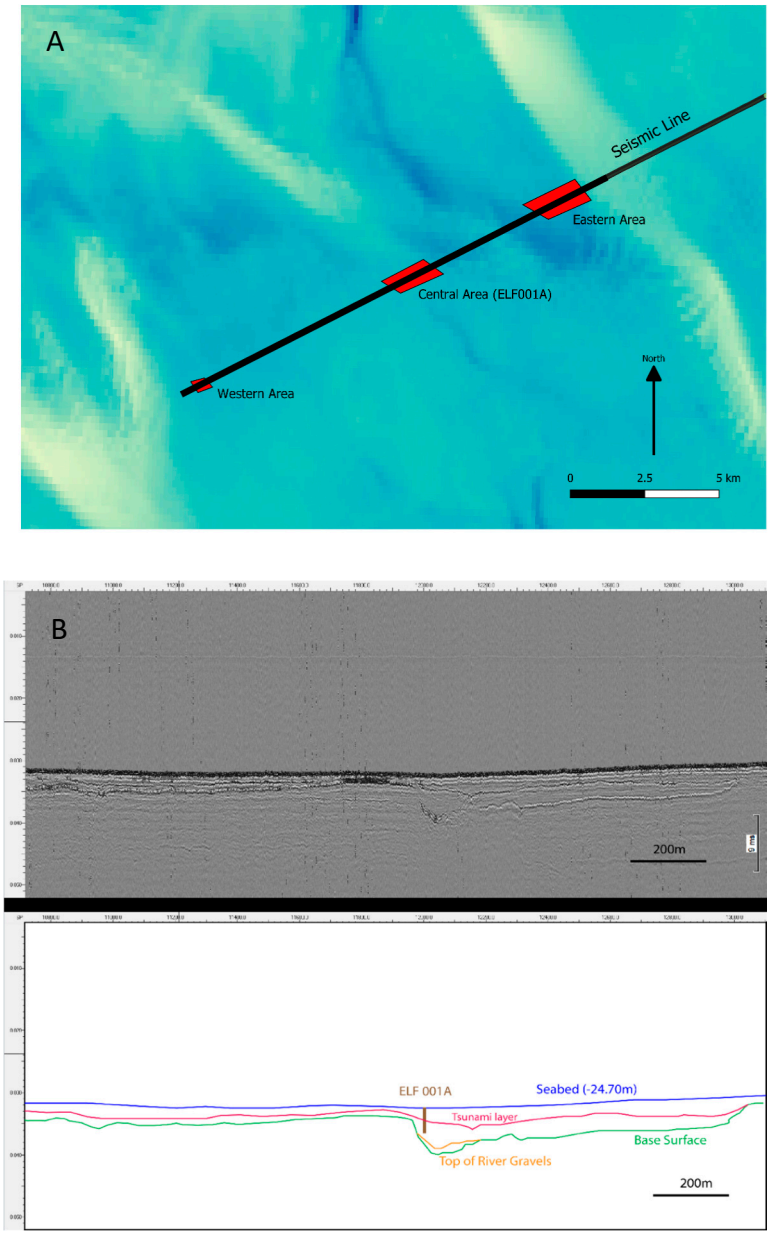

Figure S1.2 Localized discontinuous seismic tsunami signal

(A). Geographical location of seismic responses (shown in red) along the seismic survey line (shown in black) which show a similar seismic response to that shown by the Tsunami deposit at ELF001A. (B) Upper panel: 2D seismic profile of the central area over the ELF001A location. Lower panel: annotated interpretation of seismic data in upper panel.

S1.2 Core acquisition and lithographic assessment

The coring was undertaken as a dedicated survey in September 2016 by Gardline Surveys Limited. A Gardline Geosciences 5 m vibrocorer was used to collect continuous 86 mm diameter samples from 20 sites within the survey area. Opaque liners were used in all cases as optically stimulated luminescence (OSL) dating was required. The cores were sealed and wrapped in black plastic immediately upon recovery. Of the 20 sites sampled 6 required a 2nd attempt to acquire an acceptable sample. Core sites were located upon existing seismic lines to facilitate core correlation with the data. The coring locations were determined following interpretation by the archaeological team and sited over areas of archaeological interest and/or locations with potential for good archaeo-environmental preservation.

Core cutting was carried out under controlled conditions in University of Warwick laboratories. Cutting of cores and initial sampling for preserved sedimentary DNA (sedaDNA) was undertaken in environmentally controlled conditions and under red light so as to minimise likely light contamination of sediments designated for Optically Stimulated Luminescence (OSL) profiling and dating. After cutting, one half of the core was immediately sealed in black plastic for OSL dating. The other half of the core was rapidly assessed, and samples taken for specialist analyses. Core recording procedures follow the guidelines of Jones *et al*. (1999)[20]. The Basic lithostratigraphic profiles from the core logging were drawn as sections to facilitate interpretation and presented via the standard geological modelling software Rockworks (https://www.rockware.com/product/rockworks/).

The initial lithological assessment of core ELF001A revealed seven different sediment types (units) separated by sharp, abrupt or diffuse contact, Table S1, Figure S1.3. Unit ELF001A-6, characterized by structureless, loose medium sands including stones and broken

shells consistent with a storm surge, was later established to be consistent with a Storegga Slide Tsunami deposit.

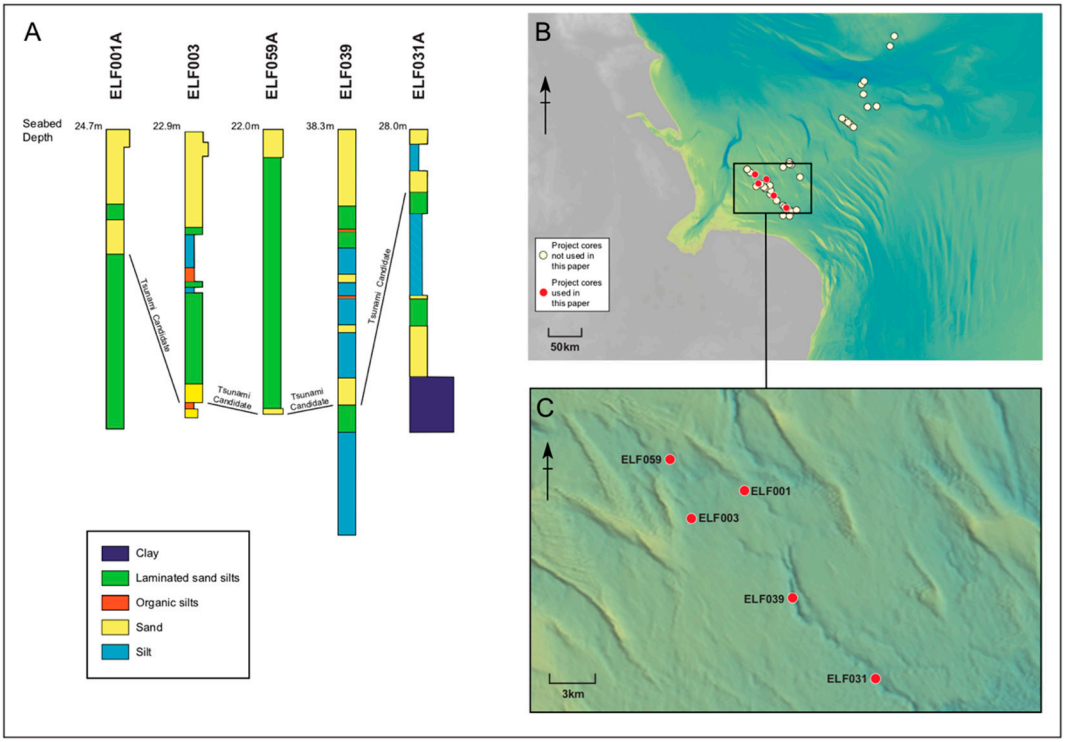

Figure S1.3 Lithography of candidate Tsunami associated cores.

A. Lithographic profiles of cores ELF001A, ELF003, ELF0031A, ELF0039, ELF0059A. B. Total sites cored in study. B. Core locations used in this study.

Depth below ground surface (m)	Depth O.D.	Lithological description	Unit Number
0.00 – 0.21		Yellow shell gravel with whole and fragmented shell. Small sub-rounded to sub-angular gravel clasts (<1cm). Structureless and loose/unconsolidated.	1A-1
		---Sharp Contact---	
0.21 – 0.67		Pale greyish yellow medium sand. Structureless. Occasional small (2-4mm) shell fragments. Some black flecks below 0.46m.	1A-2
		---Abrupt Contact---	
0.67 – 0.90		Greyish yellow medium sand with common shell fragments. Some possibly articulated Mytilus shells. Some burrowing evident, possibly very crudely bedded. Loose and unconsolidated. Some small stones.	1A-3
		---Abrupt Contact---	
0.90 – 1.09		Mid to dark grey very well laminated fine sands and silts. Predominantly sub-horizontal laminations of 2-4mm thick. Occasional dipping laminations of sand. Occasional shell fragments. Moderately cohesive.	1A-4
		---Abrupt Contact---	
1.09 – 1.19		Dark grey silty fine sand with common shell fragments. Shells are <4mm commonly but with occasional fragments larger than 3cm. Shells are broken and sharp/fresh. Possibly some crude bedding. Moderately firm and compact.	1A-5
		---Diffuse Contact---	
1.19 – 1.51		Grey medium sand with very common shells fragments including whole shells and freshly broken shell fragments. Small stones throughout unit. Loose, unconsolidated and structureless.	1A-6
		---Sharp Contact---	
1.51 – 3.50		Mid to dark grey finely laminated silts and find sands. Sub-horizontal laminations from 2-3mm thick to 1cm thick. Occasional brown organic fragments. Moderately firm and compact. Occasional sand beds 2cm thick. Possibly becoming more silty with depth.	1A-7
		---Base 3.50m---	

Table S1.1 Lithological profile of sediment core ELF001A

S1.3 Palaeobathymetry and estimation of 8.2 ka cal BP shoreline and tsunami run-up

To understand the nature of this Tsunami deposit further, the seabed bathymetry of the Southern North Sea area was recovered from the European Marine Observation and Data Network (EMODNet) data portal[12] for use in a localized reconstruction. Palaeobathymetry was created by adding isostatic adjustment data[13] to the bathymetric data obtained from EMODNet using the method identified in Hill et al. (2014)[18]. Small, unresolved islands and features associated with the presence of modern sand banks were removed from all coastlines to aid clarity and consistency. Using the method described by Fruergaard et al.[6], the local Tsunami height at ELF001A was then extrapolated from the topographic height of the top of the tsunami sequence within the core and applied to the palaeobathymetric data, Figure S1.4. It should be emphasized that the purpose of this method is not to attempt to produce a full or detailed model of the tsunami, but rather to better to generate a visualization to improve our understanding of the spatial nature of this deposit and how it arrived in the basin within which it is situated. To avoid over-fitting, from these data we inferred a more generalized interpretation of the location of the 8.2 ka cal BP coastline and the extent of tsunami run-up across the palaeolandscape by smoothing the line estimates, Figure 2.

The basin itself is an elongated structure trending North-West – South-East. It covers an area of 114 km2, with a flat bottom, gently sloping sides and is 12 meters deep. On the North, NE and NW sides of the basin, the feature is bound by terminal moraines of Late Devensian age, with tunnel valleys forming breaches in these moraine structures[14]. To the south the basin is bound by a slight topographic rise in the Boulders Bank formation. This rise is breached by a Late Devensian outwash structure which was reused in the Early Holocene by a fluvial system, referred to by the project as the 'Southern River'. Both these

breaches in the North and South West form the two main routes for material to run into or out of the basin. Using the information gained from the palaeobathymetry and the localized tsunami height, the way in which the tsunami entered the Southern River system could be ascertained. This was determined to have entered the central basin through the gap in the moraine caused by the glacial tunnel valley and outflowed through the southern section of the channel (Figure 2) was observed. We recovered cores in the southern section that contained the characteristic storm surge deposit, identifying potential tsunami material in ELF0031A, with ELF0039 as a further strong candidate for containing tsunami trace material (figures SF1.1, SF1.3, SF1.4).

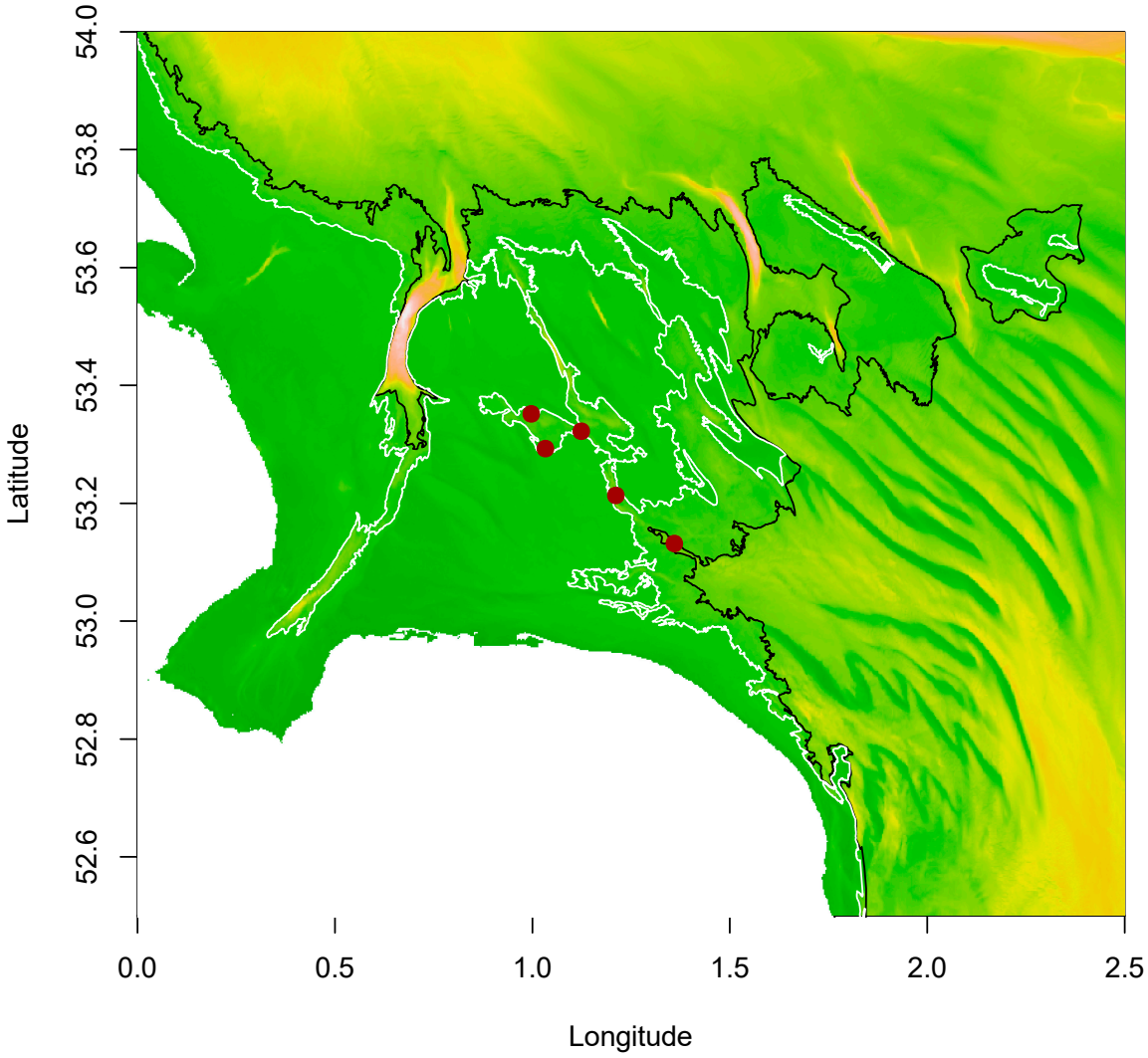

Figure S1.4 Paleobathymetric estimation of 8.2 ka cal BP coastline and tsunami run-up limit

Coastline indicated in black, tsunami indicated in white. Map coloring indicates relative bathymetric depth. Locations of candidate tsunami associated cores indicated in red circles, from left to right ELF059A, ELF003, ELF001A, ELF031A and ELF039.

Supplementary Text S2 Geophysical and Geochemical Analysis

S2.1 Palaeomagnetics

Palaeomagnetic sampling of core ELF001A was carried out at the University of Wales Trinity St David Lampeter Campus where the cores are in cold storage. Samples were taken in approximately 0.10m intervals from unit ELF001A-4 at 0.93m; 25 cylindrical samples were obtained (sample diameter 20mm) orientated up core. Samples ELF001a/1, /2 and /3 originate from the disturbed units between 0.90m and 1.51m.

Palaeomagnetic and rock magnetic measurements were carried out at the University of Bradford's Archaeomagnetic Dating Laboratory and at Lancaster University's Centre for Environmental Magnetism and Palaeomagnetism (CEMP). At CEMP the 2G Enterprises DC 755 superconducting rock magnetometer with RAPID automatic sample handler, installed in a magnetically shielded room with in-line orthogonal alternating field (AF) demagnetisation was utilised to assess the stability of the natural remanent magnetisation (NRM). All samples were subjected to stepwise AF demagnetisation peak field of 2, 4, 6, 8, 10, 15, 20, 30, 40, 50, 60, 70, 80mT. The 2G RAPID system can generate gyroremanent magnetisation (GRM) by static AF demagnetisation of ferromagnetic materials in fields above ~30mT. In order to remove this effect, basic measurement procedures set out by Stephenson (1993)[21] were followed and all results were corrected using the GRM correction tool in the software GM4Edit[22]. After each sample had undergone demagnetisation an anhysteretic remanent magnetisation (ARM) was imparted in a bias DC field of 60μT, 80μT, 100μT, 120μT applied with an in-line single axis DC coil, combined with an alternating field of 80mT. The anhysteretic magnetic susceptibility values were estimated from the slope of linear regression. Subsequently, each sample received a Saturation Isothermal Remanent Magnetisation (SIRM) at 1000mT before applying backfield IRMs at 20mT, 50mT, 100mT,

300mT, and 1000mT. IRMs were applied using a Molspin Ltd Pulse Magnetiser for 20 – 100mT and a Newport electromagnetic for 300 – 1000mT fields.

Magnetic susceptibility in the laboratory was measured using a Bartington MS2 susceptibility meter in addition to the direct measurement of the magnetic susceptibility of the core at 0.05m intervals using a Bartington MS3 susceptibility meter with MS2K attachment. Drift corrections were applied to all measurements of magnetic susceptibility. Reference should be made to Dekkers (2007)[23] for a thorough discussion on magnetic proxy parameters and their application in palaeomagnetic lacustrine settings[24,25] where similar protocols were followed. See Walden (1999)[26] for detailed discussions on ARM and it's uses as a proxy for relative abundances and magnetic grain sizes.

The magnetic properties of ELF001A are dominated by magnetite with smaller amounts of antiferromagnetic minerals more prevalent at specific horizons within the sediment. The magnetic proxy information calculated from the full suite of analyses shows four distinct magnetic phases indicative of the changing depositional palaeoenvironment.

0.90 – 1.10m Corresponding to stratigraphic unit 4 this interval lies above the tsunami event in question. From all the proxy parameters calculated this interval stands out. There appears to be a much larger abundance of magnetic minerals at this horizon as shown by the SIRM and magnetic susceptibility values. The lower percentage of IRM between 0 – 20mT signifies a lower concentration of coarse magnetite than the sediments below. This is also reflected by the ARMχ values showing a higher abundance of ultra-fine magnetite at the Superparamagnetic/Single Domain (SP/SD) boundary[25]. The S-ratio and coercivity of remanence values show a higher concentration of harder magnetic minerals such as haematite and goethite. This represents a significant change in detrital input from the

surrounding catchment compared to before the tsunami. The low %FD values (not shown) do not point to a high iron- bearing clay input as would be seen from clay rich soils. Instead the input could be from glacial till which at this time would have been deposited in the coastal area after the glacial retreat. The deposition of glacial till on the surrounding landscape could have weathered to produce haematite, as seen in similar studies of glacial retreat[27]. The increase in the transport of glacial till into this system could result in increasing trends for the magnetic concentration proxies (ARMχ, χlf, and SIRM).

1.10m – 1.50m This section relates to stratigraphic unit 6 and is the deposit associated with the tsunami event. Characterised by a much lower χlf value than the surrounding units in parallel to a drop in fine-grained magnetite (ARMχ). This suggests the material brought in by the tsunami is from a different origin to the local sediment supply as it contains a lower abundance of SP particles. The S-ratio for this phase suggests a higher concentration of haematite and goethite, however this is not mirrored by the Hard IRM proxy (not shown) or the coercivity of remanence, suggesting that the magnetic behaviour is the result of multi-domain (MD; coarser grained) magnetite co-existing with fine grained greigite. The presence of greigite particles in this deposit are indicative of intense changes in the palaeoenvironment[25].

1.50m – 1.90m This magnetic phase is distinguished by the $\%bIRM_{0\text{-}20mT}$ and the coercivity of remanence which show a larger abundance of coarse-grained magnetite up to and including the tsunami interval. At the base of this interval (~1.90m) the change in these proxies could represent the start of the glacial retreat from the southern North Sea and the gradual sea level rise. The gradual increase in ARMχ reflects the gradual increase in ultra-fine magnetite which would occur as the water column rises in conjunction with fresh glacial till deposition[25,27].

1.90m – 3.60m This phase represents little or no change in detrital input consistent with a low energy estuarine system. The S-ratio gradually increases down this part of the core suggesting a higher ratio of magnetite being deposited through this phase, which could be indicative of a change in salinity.

S2.2 Elemental core scan

The surface of each core section of ELF001A was scraped and cleaned to ensure a smooth, flat surface, and the top 3 metres was scanned using an Itrax® XRF core scanner at 500µm resolution with a dwell time of 15 seconds and x-ray tube settings at 30 kV and 50 mA. The modern material in the uppermost core section (Unit ELF001A-1) was not scanned. In individual core sections, the scanning line was adjusted to avoid sampling holes and some sub-sections were run individually to enable the core surface to be kept as flat as possible. Scanning data were compiled to produce a composite sequence. Gaps in the data represent parts of the core which were not scanned. This may have been due to sampling gaps, those instances where the nature of the sediment did not provide a smooth surface for scanning, or the result of poor data quality (low kcps values). Selected elements are presented, normalised to the sum of the incoherent and coherent scattering which account for the effects of Compton scattering and Rayleigh scattering respectively[28-30].

S2.3 Geochemical Analysis

Methodology and data QC

The surface of each core section of ELF001A was scraped and cleaned to ensure a smooth, flat surface, and the top three meters (0.21 – 3.0m) were scanned using an Itrax® XRF core scanner at 500µm resolution with a dwell time of 15 seconds and x-ray tube settings at 30 kV and 50 mA. The modern material in the uppermost core section (Lithological unit 1A-1) was not scanned. For the individual core sections, the scanning line was adjusted to avoid

sampling holes and some sub-sections were run individually to enable the core surface to be kept as flat as possible.

Elements that recorded data for all analyed depths were normalized to the sum of the incoherent and coherent scattering which account for the effects of Compton scattering and Rayleigh scattering (Chagué-Goff et al., 2017; Croudace et al., 2006 & Davies et al., 2015). Normalisation was necessary to remove any tube ageing or beam intensity factors (e.g. Fortin et al, 2012). In addition, data for individual elements were plotted by depth and if the element had >~20% analysis across the scanned core below detection the element was not taken forward for use (as it will bias principal component analysis used below). This enabled a suite of 14 elements (Si, S, Cl, K, Ca, Ti, Mn, Fe, Ni, Zn, Br, Rb, Sr & Zr) to be used to establish a chemical stratigraphy (chemostratigraphy) for the core. Furthermore, the Compton scattering data was ratioed to the Rayleigh scattering data to provide a semi-quantitative density value, Rho, for the sediment (Fortin et al., 2012). Finally, the data had a ± 5mm) moving average run over it to remove any nugget effect (that is individual spikes due to noise) produced by the fine resolution of the XRF scans (e.g. from scanning a grain >500µm).

Elements affinities

To properly establish a chemical zonation in sediment or sedimentary rocks, the likely sedimentological or mineralogical cause in any elemental change should be understood. The likely controls on elemental data presented in this study are shown in Table S2.1. As many elements are found in multiple minerals, principal component analysis (PCA) has been used to help confirm the causes of elemental variations in the core (Fig. S2.1). This increases the confidence in the elemental affiliations from Table S2.1 with detrital (Si, Ni & Zr), clay (K & Rb) , carbonate (Ca & Sr) and oxides (Mn, Fe, Ti & Zn) elements plotting in separate groups as opposed to the plotting position of Br, Cl and S.

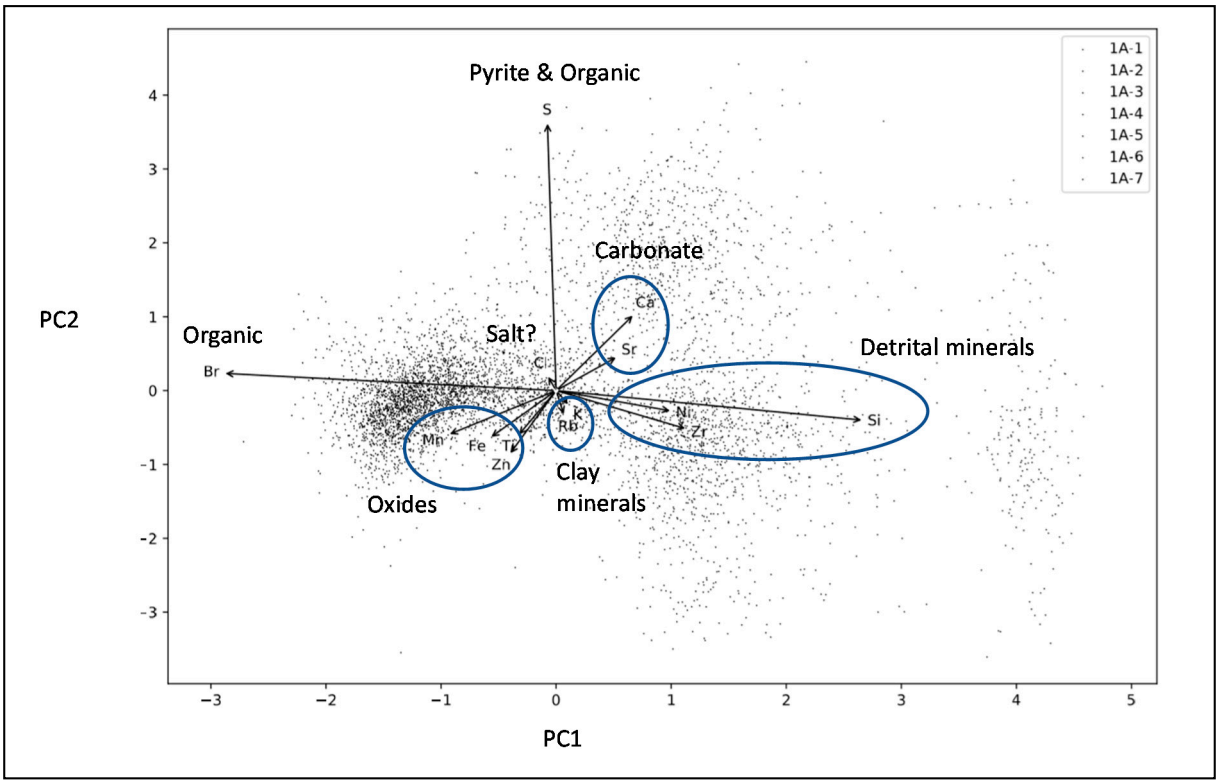

Figure S2.1 PCA of elemental affinities for ELF001A. Small black dots represent each analysed depth.

Table S2.1 Elements analysed from core scanning. [1]- Croudace et al.(2006), [2] –Thompson et al. (2006) [3]- Chagué-Goff et al. (2017).

Element	Control on abundance
Si	Quartz[1]
Ni	Deep sea FeMg silicates and oxides[1]
Zr	Zircon (terrestrial heavy minerals)[1]
K	Illite[1]?
Rb	Clay minerals[1]
Ca	Carbonate[1]
Sr	Aragonite[1]
Mn	Mn Oxides[1]
Fe	Secondary hydrous oxides [1]
Ti	Detrital oxides[1]
Zn	Ferromagnesian silicates & detrital oxides[1]
Br	Organic[2]
S	Pyrite, Organic[1,2] & marine influence [3]
Cl	Salt[2]

To produce a chemical zonation and further the understand the depositional setting ELF001A, three key elemental proxies were selected:

- Sr/Rb – Marine/Clay sediment (chemical proxy for Aragonite i.e. shell/Clay; e.g. Chagué-Goff et al., 2017)
- Si/Rb – Grain size (chemical proxy for Quartz/Clay; e.g. Chagué-Goff et al., 2017)
- Zr/Sr - Terrestria/Marine sediment (chemical proxy for detrital zircons)/Marine sediment (e.g. Chagué-Goff et al., 2017)

Chemical zonation

The ratios were used to subdivide ELF001A into six units (Figure S2.2). The uppermost (youngest) C2 and lowermost (oldest) C7. All described changes in data refer to an upward change in chemistry.

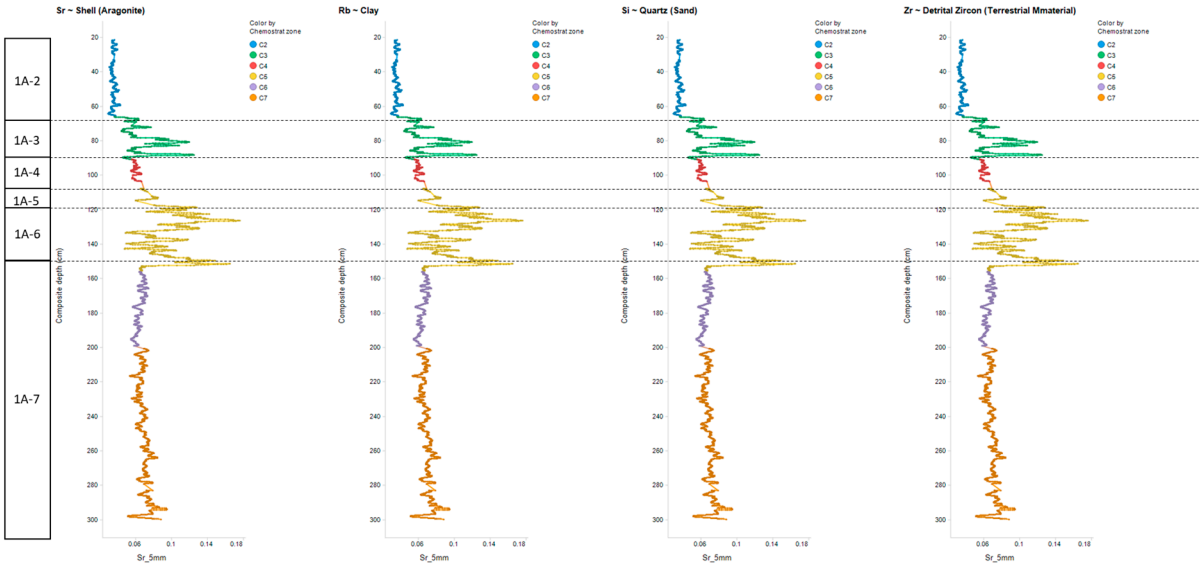

Figure S2.2 Chemical zoning of ELF001A based on core scan geochemistry, specifically on Sr/Rb (Shell/Clay), Si/Rb (Quartz/clay), & Zr/Sr (Terrestrial/Marine sediment). See Croudace et al. (2006) Thompson et al. (2006) & Chagué-Goff et al. (2017). 1A-2 to 1A-7 refer to lithostratigraphic zones (see supplementary information SI1.1)

Unit C7

- Sr/Rb Low ~2.5
- Si/Rb Low ~0.3, however there are multiple small zones with elevated Si/Rb values up to ~1.
- Zr/Sr Low ~0.6

Interpretation:
A clay/silty unit with interbedded siltier horizons (marked by increases in Si/Rb). Little shell material with small amounts of shell material in the lowermost 2 beds (marked by Sr/Rb peaks). Little shell material and a constant balanced marine/terrestrial influence.

C7/C6 boundary

A decrease in Si/Rb.

Unit C6

- Sr/Rb Low ~2.5
- Si/Rb Very Low ~0.2
- Zr/Sr Low ~0.6

Interpretation:
The lowest energy unit in ELF001A dominated by clay material. Little shell material and a constant balanced marine/terrestrial influence.

C6/C5 boundary

A large and sharp increase in Sr/Rb, Si/Rb and a decrease in Zr/Sr.

Unit C5

- Sr/Rb Very high and variable, ranging from ~18-3

- Si/Rb High and variable, ranging from ~2.3 to .7
- Zr/Sr ~ 0.4 Low but with high peaks up to 1.4

Interpretation:

The very sharp rise in Sr & Si suggest an unconformable boundary to a high energy/coarser material including shell/marine material. The low Zr/Sr ratios also suggest this unit is dominated by a marine influence. The large variation in data within C5 does suggest internal sedimentary architecture (discussed below). Internally the high variation in data. The top of this unit shows a grading change back to values similar to those in units C6&7. These observations suggest this may either be a tsunami or surge deposit; an erosive base, high energy deposit bringing distal marine sediment into a previously terrestrially dominated low energy environment topped by a gradational decrease of energy.

C5 internal structure:

The high resolution capture of the geochemical data across the zone C5 enables the identification of eight internal sub-zones (a to h; Figure S2.3).

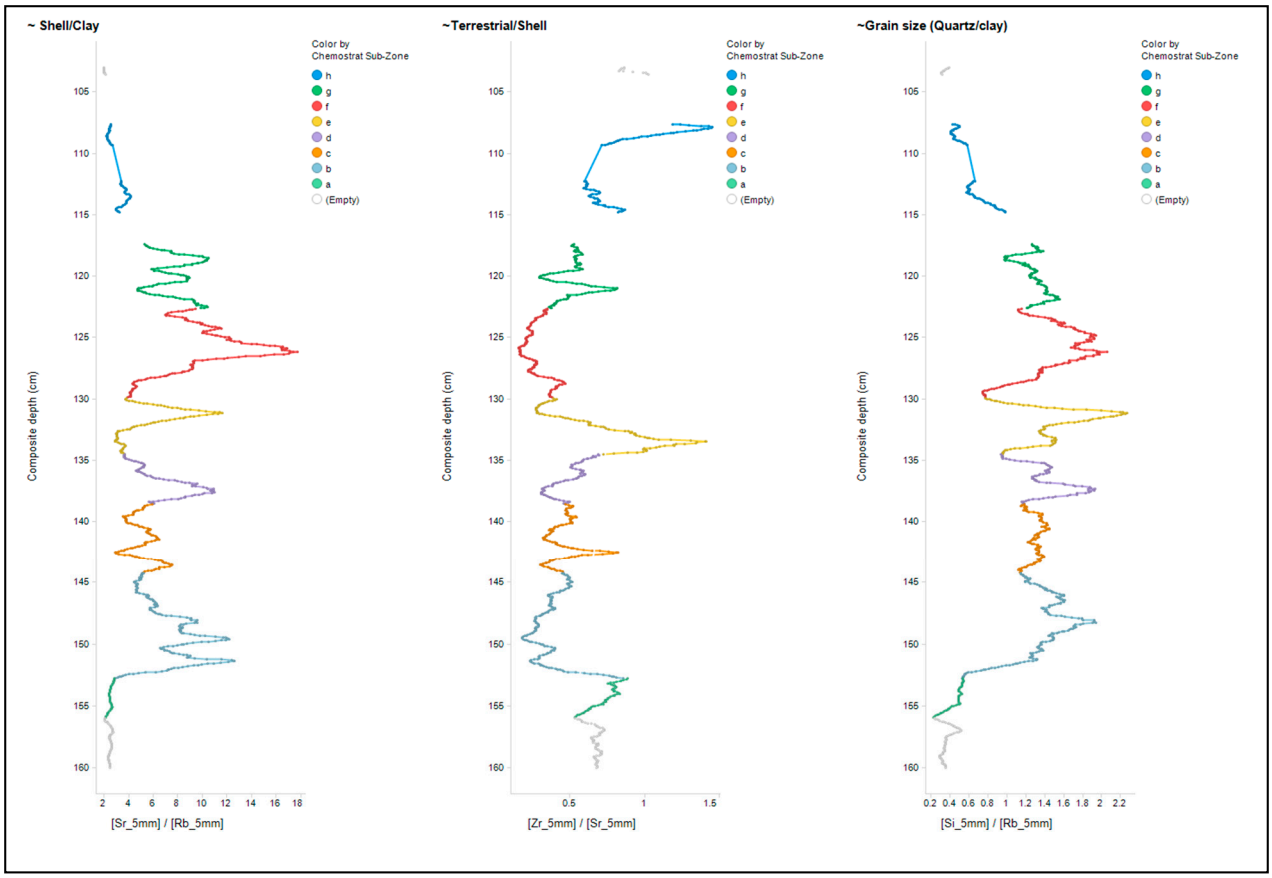

Figure S 2.3 Geochemical sub-zones for Unit C5 showing internal structure.

- Sub-zone a is identified by an increase in Zr/Sr
- Sub-zones b to h:

    - Identified by repeated cycles of Si/Rb, increasing at the base, peaking in the middle of the zone and then decreasing towards the top. The boundary between zones a to h are picked on the minimum Si/Rb Values.
    - Sub-zones b, d & f have higher Sr/Rb peaks than zones c, e & g
    - Sub-zones c, e, & g have higher Zr/Sr peaks than zones b, d & f
- Sub-zone h is identified by an increase in to the highest Zr/Sr values within C4 and continued decrease back to minimum Si/Rb values.

Interpretation:

The identification of chemostrat sub-zones a-h supports the hypothesis that sediment from ~1.05m to ~1.55m depth in core ELF001A are a tsunami deposit and provide an internal architecture for the tsunami of an initial sea level fall followed by three wave packages that each contain an inward moving wave and a retreating seaward backwash with each topped by a clay rich cap (Figure S 2.3).

- Initial sea level fall is identified by the increase in energy and terrestrial material in sub-zone a.
- Tsunami waves 1-3 each (zones b-g) possess an inland and seaward pulse identified through increasing energy at the base of each pulse, peaking in the centre then then fining up to the top of each pulse. The inland propagating pulse (b, d & f) are identified by having a greater shell/marine signal at their peak, whereas the seaward propagating pulses (c, e & g) are identified by possessing more terrestrial material at their peak.
- The uppermost sub zone is identified by a decrease in energy and grain size, forming a clay cap at the top of the unit (h).

The identification of both inward wave and outward backwash in each pulse within unit C4 is highly suggestive of a tsunami rather than storm surge as indicated by Kortessa and Dawson (2007), Morton et al. (2007) and Peters and Jaffe (2010).

Unit C4

- Sr/Rb Low ~2.2
- Si/Rb Low-moderate ~0.5
- Zr/Sr Moderate ~ 1

Interpretation:

A return to the previous clay/silt environment seen in units C5&6 with no shell material, however the moderate Zr/Sr values suggest a more terrestrial input compared to Units C5&6.

C4/C3 boundary

A sharp increase in Si/Rb and Sr/Rb values, no change in S/Rb.

Unit C3

- Sr/Rb Moderate (~3) with three spikes up to ~10
- Si/Rb High ~1.8
- Zr/Sr Moderate ~1 with high peaks ~2.5

Interpretation:

A high energy interbedded terrestrial sand and marine/shell dominated deposit.

C3/C2 Boundary

A reduction in Sr/Rb and increase in Si/Rb.

Unit C2

- Sr/Rb Low ~2.2
- Si/Rb Very high ~2.2
- Zr/Sr Moderate ~1 with very high peaks up to ~5

Interpretation

A cleaner high energy sand with no shell/marine material or marine influence. Several beds display high Zr/Sr values suggesting increased terrestrial derived heavy mineral sand beds.

Summary & comparison with other datasets.

A summary of the geochemical interpretation of the tsunami zone is given in Figure S2.4 and Table S 2.2.

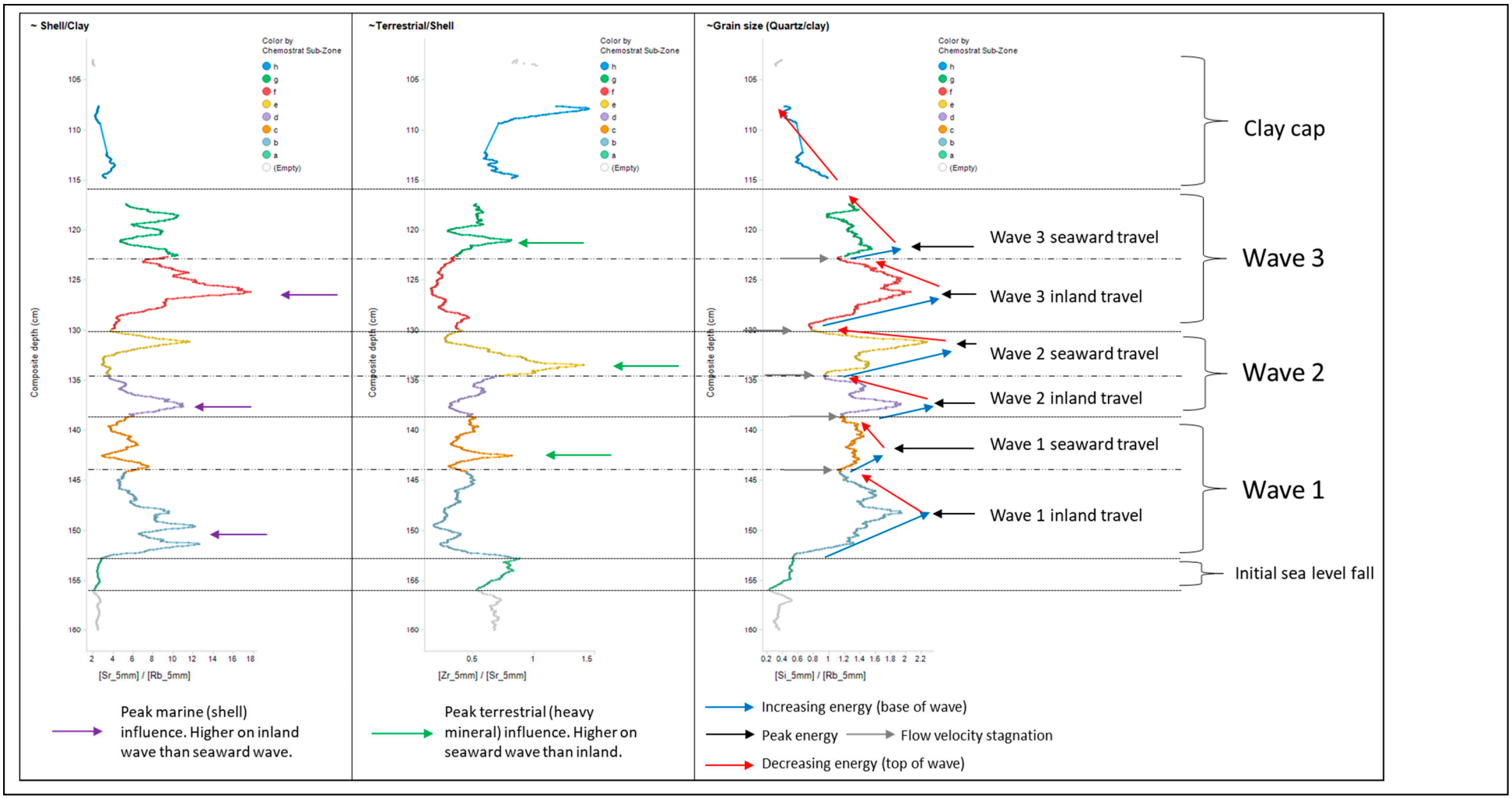

Figure S2.4 Summary of geochemical signatures across zone C5, interpreted as the result of the tsunami.

Chemostrat Zone	Chemostrat Sub-zone	Top Depth (m)	Key geochemical marker			Interpretation	Equivalent zone			
			Sr/Rb Marine material (Shell)/Clay	Si/Rb Grain size & Energy (Quartz/clay)	Zr/Sr Terrestrial/Marine sediment input (Detrital zircon/Shell)		Lithostrat Unit	Lithostrat description	Ecological	OSL Inference
C2	-	0.22 (top analysed sample)	V. low (2.2)	v high (2.2)	moderate (1, peaks 5)	High energy sand, no shell or marine influence - increased terrestrial signature	1A-2	Yellow sand with common shell fragemnts	-	Recent Sands
Contact			reduces	increases		Gradual, reduced Sr/Rb and increasing Si/Rb				
C3	-	0.66	moderate (3, peaks to 10)	high (1.8)	moderate (1, peaks 2.5)	Increasing sand and marine shell, interbedded deposit with increased energy	1A-3	Yellow sand with shell fragments	-	-
Contact						sharp increase in Si/Rb and Sr/Rb				
C4	-	0.91	low (2.2)	moderate (0.5)	moderate (1)	silt dominated, low energy but with increased terrestrial input with higher Zr/Sr values	1A-4	Fine sands and silts	Esturine Mudflats	Tidal Mudflats
Contact			-	End of decrease	-	Minimum energy				
C5	h	1.08		Decreasing to minimal value	Increasing	Return to very low energy environment with increased terrestrial signal - return to pre tsunami similar conditions	1A-5	Sand with large shell fragments	Tsunami w. saltmarsh fossils	Tsunami 2 (waning)
	Contact		-	decreasing	-	Increase in Si/Rb				
	g	1.17			Peak in centre of zone	Increased terrestrial material - seaward return wave 3	1A-6	Unconsolidated sand with common whole and freshly broken shell fragments and small stones	Tsunami	Tsunami 1
	Contact		-	End of decrease	-	Flow velocity stagnation				
	f	1.23	Peak in centre of zone			Increases shell and marine material - inland wave 3				
	Contact		-	End of decrease	-	Flow velocity stagnation				
	e	1.30			Peak in centre of zone	Increased terrestrial material - seaward return wave 2				
	Contact		-	End of decrease	-	Flow velocity stagnation				
	d	1.35	Peak in centre of zone			Increases shell and marine material - inland wave 2				
	Contact		-	End of decrease	-	Flow velocity stagnation				
	c	1.40			Peak in centre of zone	Increased terrestrial material - seaward return wave 1				
	Contact		-	End of decrease	-	Flow velocity stagnation				
	b	1.44	Peak in centre of zone			Increases shell and marine material - inland wave 1				
	Contact		-	End of decrease	-	Flow velocity stagnation				
	a	1.53	-	High (variable, >0.7)	Increasing	Increased terrestrial input - water retreat?	1A-7	Mid to dark grey laminated silts and fine sands	Estuarine Mudflats & Algae	Tidal Mudflats
Contact			Dramatic increase		Decrease	Erosive base, major increase in energy				
C6	-	1.56	low (2.5)	v. low (0.2)	low (0.6)	Clay dominant, minimal shell, balanced marine input, low energy environment				
Contact			constant	decrease	constant	Decreasing energy				
C7	-	2.00	low (2.5)	low (0.3, peaks to 1)	low (0.6)	Clay rich with interbedded siltier horizons, occasional shell at base				

Table S2.2 Summary table summarising chemostratigraphic units & sub-units tops, their geochemical markers and Interpretation. It also compares Chemostratigraphic zones with the equivalent Lithostratigraphic, Ecological and OSL zones and their interpretation, displaying a good conformity between techniques.

Table S2.2 compares the chemostratigraphy and chemical data compared to the lithostratigraphy, ecology and OSL results for ELF001A, all of which are in good agreement. The clay rich chemo units C7 & C6 correspond to lithostratigraphy unit 1A-7 and the estuarine mudflat ecological interpretation. C5 corresponds to lithostratigraphy unit 1A-6 and the interpreted tsunami deposit in the ecology data. Furthermore, there is an excellent agreement (taking account of the different sampling resolutions) between the chemically and OSL identified sequence. The final sub-zone h also corresponds to the separate ecological tsunami zone with saltmarsh fossils, lithostratigraphy unit 1A-5 and the waning wave identified in the OSL data. Chemical unit C4 corresponds to lithostratigraphy unit 1A-4 and a return to mudflat fossils. Lastly, chemo zones C3 & C2 correspond with lithostratigraphic zones 1A-3 & 1A-2 respectively.

Finally, it is possible to calculate the density of the analysed sediment by normalising the Compton and Rayleigh scattering reported by the Itrax XRF (Fortin et al., 2012; Figure S2.5). This shows a sharp decrease from ~3.2 (approximate density of clays) to ~2.7 (approximate density of quartz) across the C6/C5 boundary which it is expected twill be visible on seismic. This likely confirms that the main seismic reflector is recording the erosional base of the tsunami.

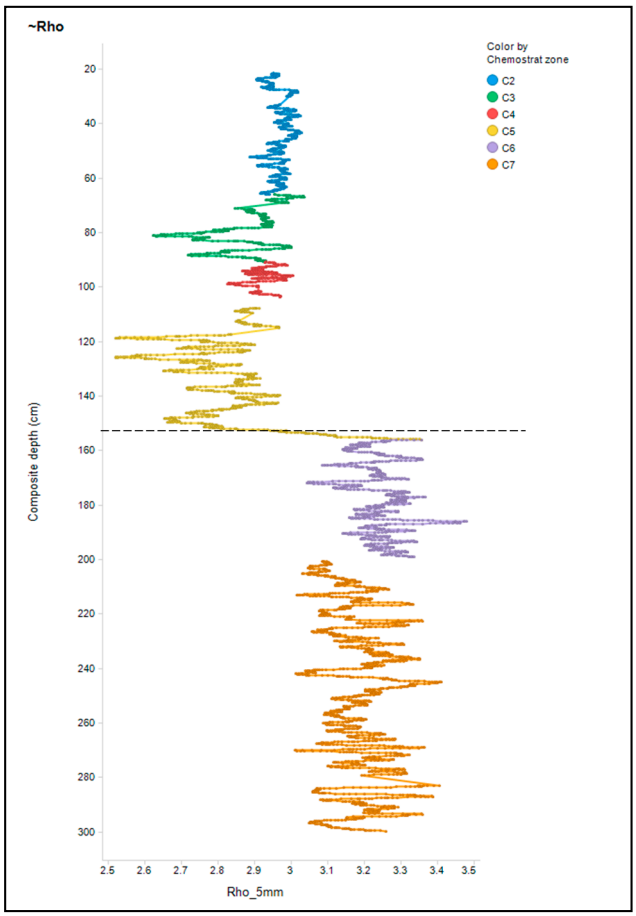

Figure S2.5 Density calculation based on geochemical data

References

Chagué-Goff, C., Szczuciński, W., Shinozaki, T. 2017 Applications of geochemistry in tsunami research: A review, Earth-Science Reviews, 165, (203-244), (2017)

Croudace, I., Rindby, A., Rothwell, R., 2006. ITRAX: description and evaluation of a new multi-function X-ray core scanner. In: Rothwell, R. (Ed.), New Techniques in Sediment Core Analysis. Geological Society, London, pp. 51–63

Davies, S.J., Lamb, H.F., Roberts, S.J., 2015. Micro-XRF core scanning in palaeolimnology: recent developments. In: Croudace, I.W., Rothwell, R.G. (Eds.), Micro-XRF Studies of Sediment Cores. Springer, Netherlands, pp. 189–226.

Fortin, D., and the The PASADOScience Team. 2012. Destructive and non-destructive density determination: method comparison and evaluationfrom the Laguna Potrok Aike sedimentary record, Quaternary Science Reviews, v71, pp. 147-153.

Kortekaas, S. and Dawson, A. G. 2007. Distinguishing tsunami and storm surge: An example from Martinhal, SW Portugal. Sedimentary Geology, v. 200, pp. 208-221

Morton, R. A., Gelfenbaum, G. and Jaffe, B. E. 2007. Physical criteria for distinguishing sandy tsunami and storm deposits using modern examples. Sedimentary Geology, v. 200, pp. 184-207

Peters, R., and Jaffe, B. E., 2010, Identification of tsunami deposits in the geologic record; developing criteria using recent tsunami deposits: U.S. Geological Survey Open-File Report 2010-1239, 39 p.

Thompson, J., Croudace, I.W. & ROTHWELL, R.G. 2006. A geochemical application of the ITRAX scanner to a sediment core containing eastern Mediterranean sapropel units In: Rothwell, R. (Ed.), New Techniques in Sediment Core Analysis. Geological Society, London, pp. 65-77

S2.4 Organic Chemistry profiling: An Agilent 7890A gas chromatograph (GC) coupled with a 5975C Inert XL mass selective detector was used for the lipid analysis. The splitless injector and interface were maintained at 300°C and 340°C respectively. Helium was the carrier gas at constant flow. The temperature of the oven was programed from 50°C (2 min) to 350°C (10 min) at 10°C/min. The GC was fitted with a 30m x 0.25mm, 0.25µm film thickness 5% Phenyl Methyl Siloxane phase fused silica column. The column was directly inserted into the ion source where electron impact (EI) spectra were obtained at 70 eV. Samples were analyzed using a full scan method from *m/z* 50 to 800. For the lipid extraction, fourteen sub-

samples from core ELF001A were dried at room temperature for 48 hours,~3g of each was then solvent extracted using three portions of 12ml (dichloromethane: methanol 2:1 v/v) with ultrasonication and centrifugation. The solvent was transferred into a clean glass vial and removed under a stream of nitrogen at 40°C. The extracts were then silylated with ~5 drops of BSTFA at 70°C for an hour. Excess BSTFA was removed under a stream of nitrogen and the samples diluted in 1ml of dichloromethane for analysis.

The lipids analysis of core ELF001A, yielded *n*-alkanes, fatty acids, *n*-alkanol and sterols, of these lipids the *n*-alkanes are the most informative in respect of the origin of the lipids. These show that; the area ELF001A -3 is dominated by marine organic inputs probably from submerged aquatic plants. In area ELF001A -4, aquatic plants are present, with the signals for bacteria and terrestrial plants in significant quantities. In addition, signals of sulfate reducing bacteria were also identified. This area has the chemical profile of an estuarine area, or it may be an area of water present, just before submergence. Area ELF001A -5 has a chemical organic profile similar to that obtained from area ELF001A -3, where submerged marine plants are dominant. In contrast, area ELF001A -6 is the most complex portion with evidence for terrestrial and marine plants and algae within just 15cm of the column, although marine inputs dominate this area. This suggests a major event associated with the deposition of these mixed deposits within well-defined strata. Area ELF001A -7 is the most homogenous of samples examined and is associated with terrestrial plants, bacteria and freshwater within the lower part of the core. The Carbon Preference Index CPI ratio for these samples distinguishes between terrestrial and marine sources. This indicates that terrestrial materials are increasingly present in the lower parts of the core[31,32] (Figure 3). All

NAR ratios are closer to one than zero, which indicates the origin of the lipids from sources other than petroleum[33,34] (Figure 3).

Supplementary Text S3 Sediment dating

S3.1 OSL dating of sediments

In this supplementary text, we describe the protocols and procedures that were used to determine the quartz SAR OSL ages shown in Table S3.1.

Table S3.1 OSL date summary of sediment core ELF001A

Unit no.	Description / context	Sample ID / CERSA no.	Age / ka
4	**laminated fine sands and silts; estuarine mudflats – open marine**	114/21, 114/22	6.03 ± 0.22
		114/23	**7.16 ± 0.50**
5	grey silty fine sands, with shells; tsunami deposit	114/24, 114/25	8.22 ± 0.43
6	grey medium sands, v common shell fragments, small stones; tsunami deposit	114/29, 114/30, 114/31, 114/32	8.04 ± 0.43
5 & 6	**tsunami deposit**	**114/24, 114/25, 114/29, 114/30, 114/31, 114/32**	**8.14 ± 0.29**
7	mid to dark grey finely laminated silts and fine sands; **estuarine mudflats – restricted marine**	**114/33**	**9.17 ± 1.47**

S3.1.1 Luminescence screening measurements (Figure S3.1)

The sediments revealed in core ELF001A were first appraised using portable OSL equipment (following procedures reported in Sanderson and Murphy, 2010 and Kinnaird et al., 2017). This allowed for the calculation of IRSL and OSL net signal intensities, their depletion indices and the IRSL - OSL ratio, which were plotted in relation of the lithostratigraphy of the core (Figure S1.1). This proxy information was used to select the most promising intervals in the core for dating: at the base of the *open marine* estuarine mudflats (unit 4), through the tsunami deposit (units 5 and 6), and at the top of the *restricted marine* estuarine mudflats (unit 7).

S3.1.2 Calibrated luminescence measurements (figures S3.1 and S3.2)

Calibrated luminescence screening methods, as previously utilised by Kinnaird et al. (2017)[35] were used to generate stored sensitivity- and dose-depth profiles for core ELF001A. Luminescence sensitivities (photon counts per Gy) and stored dose (Gy) were evaluated on paired aliquots of HF-etched quartz, using procedures modified from Burbidge et al. (2007)[37], Sanderson et al. (2003)[38] and Kinnaird et al. (2017)[35]. This calibrated dataset is shown relative to the proxy information and the lithostratigraphy in Figure S3.1.

All OSL measurements were carried out using either Risø TL/OSL DA-20 or DA-15 automated dating systems, equipped with a $^{90}Sr/^{90}Y$ β-source for irradiation (dose rates at time of measurement, 1.10 and 0.03 Gy/s, respectively), blue LEDs emitting around 470 nm and infrared diodes emitting around 830 nm for optical stimulation. OSL was detected through 7.5 mm of Huoya U-340 filter and using a 9635QA photomultiplier tube. OSL was measured at 125°C for 60 s. The OSL signals, *Ln* and *Lx*, used for equivalent dose (*De*) determinations were obtained by integrating the OSL counts in the first 2.4 s and subtracting an equivalent signal taken from the last 9.6 s. The protocol implemented here involved a readout of the natural signal, followed by a 1 Gy test dose, then readouts of the regenerated cycles following a series of nominal doses between 5 and 120 Gy, each with a subsequent 1 Gy test dose. For all, OSL followed a preheat of 220°C and was measured at 125°C for 60s.

Apparent dose estimates were made in Luminescence Analyst v.4.31.9, using dose response curves forced through zero and the two to three normalized regenerative points with an exponential function (Figure S3.2).

S3.1.3 Equivalent dose determinations (figures S3.3 to S3.5)

Samples selected for full quantitative quartz OSL dating were subjected to further mineral purification of quartz (cf. Kinnaird et al. 2017)[35]. Equivalent doses were determined by OSL on at least 20 aliquots per sample (typically 40+ aliquots) using a single aliquot regenerative dose (SAR) OSL protocol (cf. Murray and Wintle, 2000[39]; Kinnaird et al. 2017[35]; see S3 therein). This was implemented, using five regenerative doses (nominal doses between 1 and 40 Gy), with additional cycles for zero dose, repeat or 'recycling' dose (2.5 Gy) and IRSL dose (2.5 Gy). Five preheat temperatures were explored between 220 and 260°C, in 10°C increments.

Data reduction and De determinations were made in Luminescence Analyst v.4.31.9. Individual decay curves were scrutinised for shape and consistency. Dose response curves were fitted with an exponential function, with the growth curve fitted through zero and the repeat recycling points. Error analysis was determined by Monte Carlo Stimulation.

The equivalent dose distributions for each sample are shown relative to the lithostratigraphy of the core in figures S3.3 and S3.4, for the grain size fractions 90-150µm and 150-250µm (see also tables S3.2 and S3.3). Individual sample distributions were appraised for equivalent dose homogeneity, and, when the luminescence profiles suggested stratigraphic coherence, different combinations of merged datasets across stratigraphic associations were explored (e.g. Fig. S3.5). Different permutations of the assimilation of equivalent doses to obtain the burial dose were considered, including weighted combinations and statistical dose models[40]. It was concluded that, with the dosimetry as presently constrained, the combined distributions were most appropriate for calculation of the stored dose. In justification of this, the stored doses thus obtained correlate well with the apparent dose-depth profiles obtained earlier ($R^2 = 0.943$).

S3.1.4 Dose rate determinations (Figure S3.6)

The dose rates to these materials were assessed through a combination of X-ray Fluorescence core scanning, high-resolution gamma spectrometry (HRGS), and inductively-coupled plasma mass spectrometry (ICPMS) analysis.

Semi-quantitative element concentrations of K, U and TH, as obtained by X-ray Fluorescence core scanning at Aberystwyth University are shown in Figure S3.6.

HRGS measurements were performed at the Environmental Radioactivity Laboratory (ERL; UKAS Testing Lab 2751), University of Stirling. All sample handling, processing and analysis were undertaken in accordance, and in compliance with ERL protocols LS03.1, 03.2 & 03.6 and LS08. HRGS measurements were performed on a High Purity Germanium detector. Standard laboratory efficiency calibrations were used, derived from GE Healthcare Ltd QCY48 Mixed Radionuclide Spike and DKD RBZ-B44 ^{210}Pb spike. All absolute efficiency calibrations were corrected for variations in sample density and matrix. HRGS measurements were undertaken on composite bulk sediment samples at 108cm, 150cm, 155cm and 360cm.

Radionuclide concentrations determined by HRGS are listed in Table S3.4.

Concentrations of K, U, Th and Rb were measured directly using ICPMS at the STAiG istope labs at the University of St Andrews. ICPMS measurements were performed on dried, homogenised sub-samples of sediment taken from discrete horizons in the core. 15-20 g of sediment were taken from each sample, then ground and homogenised using a Tema Machinery Disc Mill. 2 gram sub-samples were treated in a furnace set at 1000 °C for 6 hours. 50 mg quantities of sediment from each sub-sample were prepared for ICPMS using total rock digestion by Ammonium Bifluoride[41], adapted to include additional fluxes in hot

HCl and HNO_3. Samples were prepared by gravimetric serial dilution at 10 and 1000x in 0.4 M HNO3:0.02 M HF, for analysis of U and Th, and K, respectively. All analyses were conducted on an Aligent 7500 ICP-MS instrument. Samples and standards were introduced through a PFA spray chamber in 0.4 M HNO3:0.02 M HF using a self-aspirating nebuliser (100 µL min-1). Analytical calibration standards (0.1, 1, 10, 100 and 500 ppb for all elements) were prepared by gravimetric serial dilution from 10 ppm certified stock multi-element solutions (Agilent) in 0.4 M HNO3:0.02 M HF. Inter-calibration between counting and analogue detection modes was performed prior to each analytical session. ICPMS analyses were performed on samples CERSA119 [95-100cm depth], 114/21-22 [100cm], 120 [100-105cm], 122 [110-117cm], 114/28-29 [129-136cm], 114/31-32 [146-150cm], 114/33-34 [155-160cm], 114/35-36 [165-170cm] and ELF114/4-45 [201-211cm]. An IAG reference material, SdAR-L2 blended sediment, was prepared and run in batch with the ELF001A core samples. Analytical calibration standards (0.1, 1, 10 and 100 ppb for all elements) were prepared by gravimetric serial dilution from 10 ppm certified stock multi-element solutions (Agilent) in 0.4 M HNO3:0.02 M HF. Additional calibration standards at 2 and 75 ppb were prepared and run as 'samples' within the sample batch.

Radionuclide concentrations determined by ICPMS are listed in Table S3.5.

These data were used to determine infinite matrix dose rates for α, γ and β radiation, using the conversion factors of Guérin et al. (2011)[42], grain-size attenuation factors of Mejdahl (1979)[43] and attenuated for sediment-matrix water contents. Table S3.6 lists the effective beta, gamma and total environmental dose rates to HF-etched, 90-150µm quartz.

S3.1.5 Age determinations

Luminescence ages are calculated as the quotient of the stored dose (or burial dose, Gy section C above) and the environmental dose rate to these materials (mGy a^{-1}; section D; Table S3.7). The resolution at which the stored doses were constrained (at 5 to 10 cm through the tsunami deposit) is not matched by the resolution at which the dosimetry is constrained (>15 cm). From the core scan it is known that there are significant variations in K concentrations within the tsunami deposits, with positive and negative gradients and also spikes. It was thus concluded that combining equivalent doses from each of the units - 4, 5, 6 and 7 – provided the most appropriate method of assimilation for calculating depositional ages. The results of these determinations support a link to the Storegga tsunami and are coincident with dating for this event between 8120 -8175 cal BP, provided through other studies[44-46].

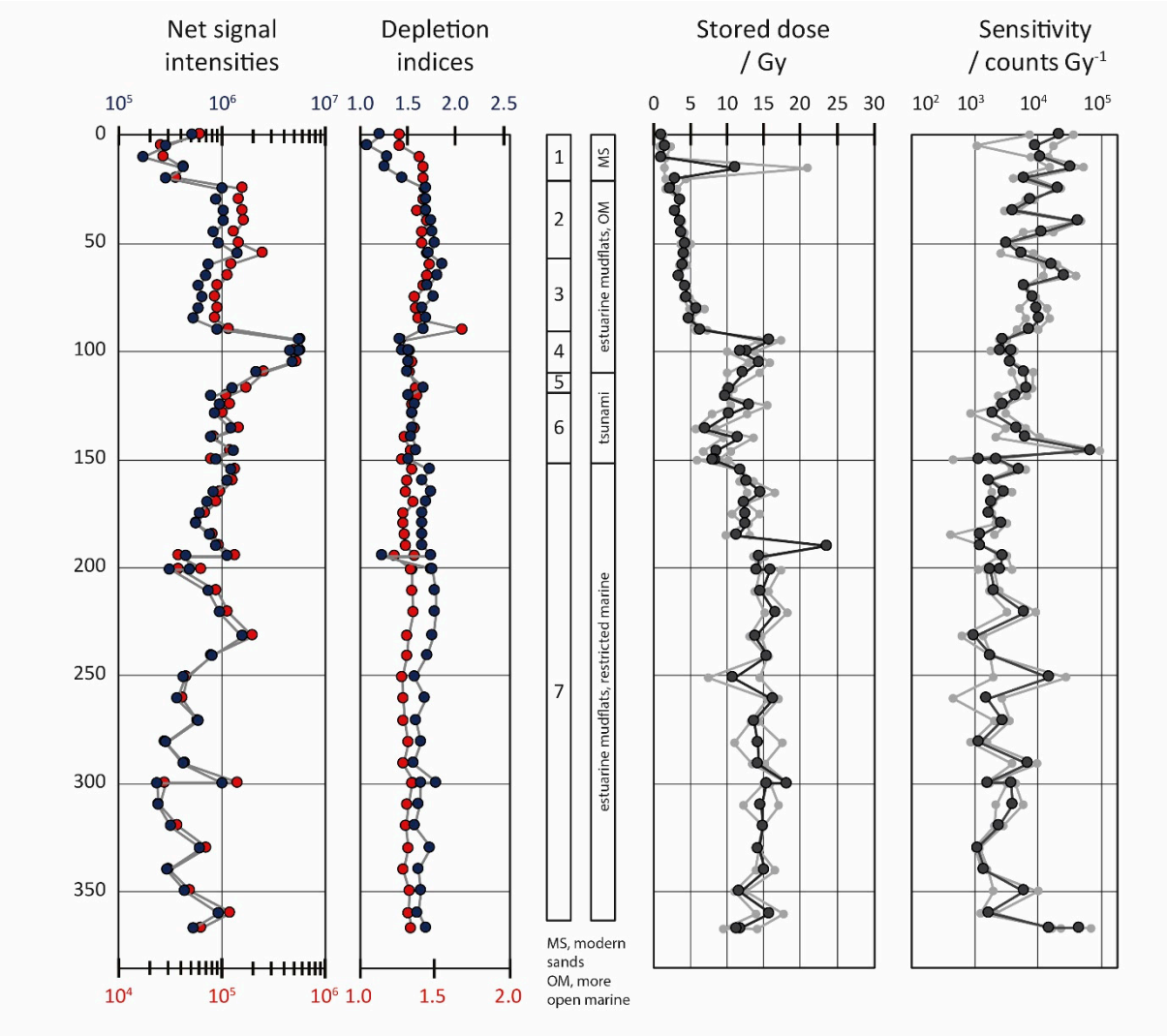

Figure S3.1: Luminescence stratigraphies for ELF001A: (left) proxy luminescence- depth profile generated at sampling using portable OSL equipment, (right) stored dose- and sensitivity- depth profiles based on a simplified SAR OSL on paired aliquots of HF-etched quartz

a. CERSA114/21 (unit 4)

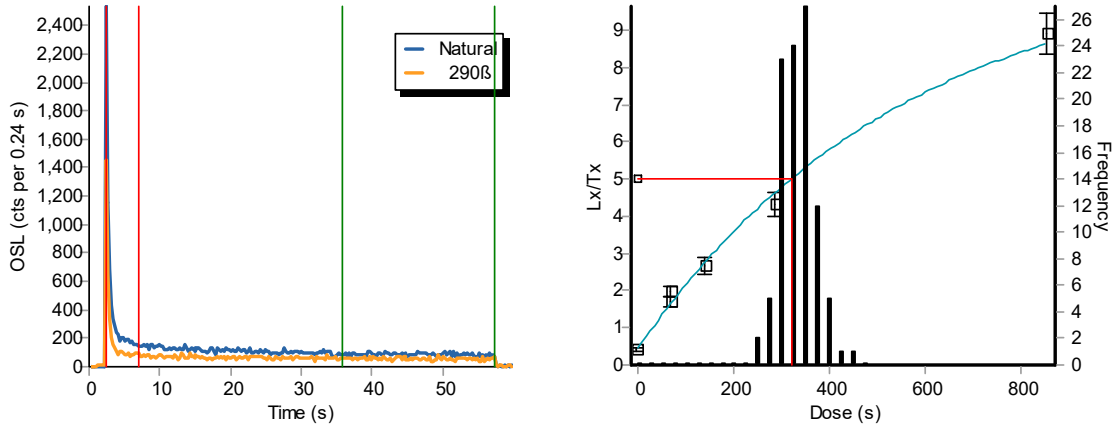

b. CERSA114/25 (unit 5, top)

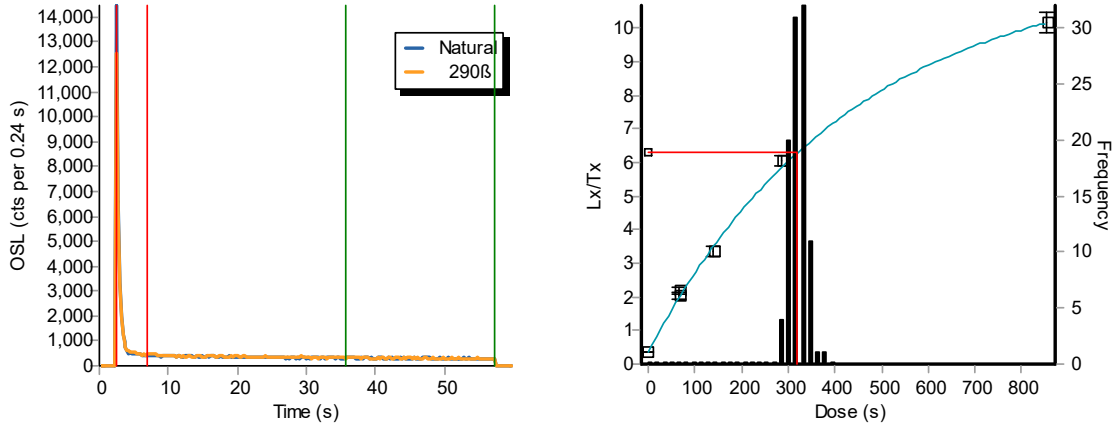

c. CERSA114/31 (unit 6, base)

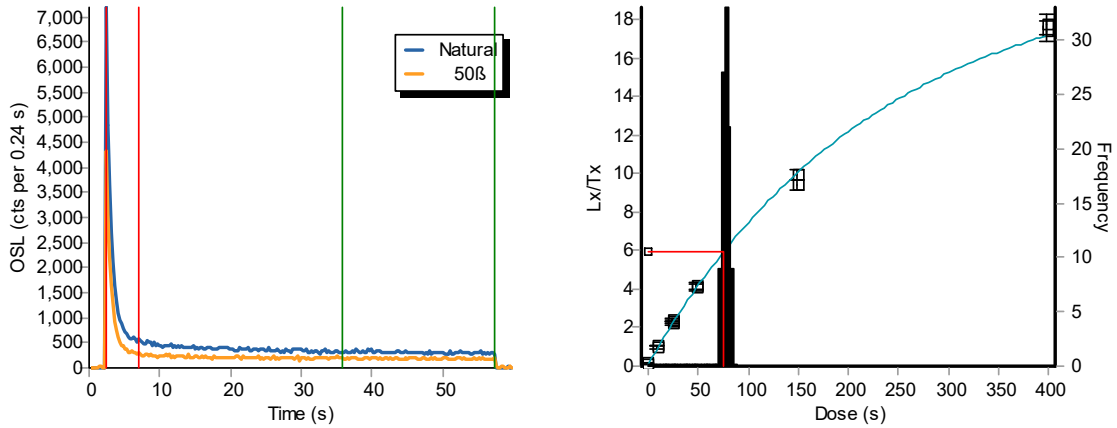

Figure S3.2: Representative decay (left) and composite dose (right) curves

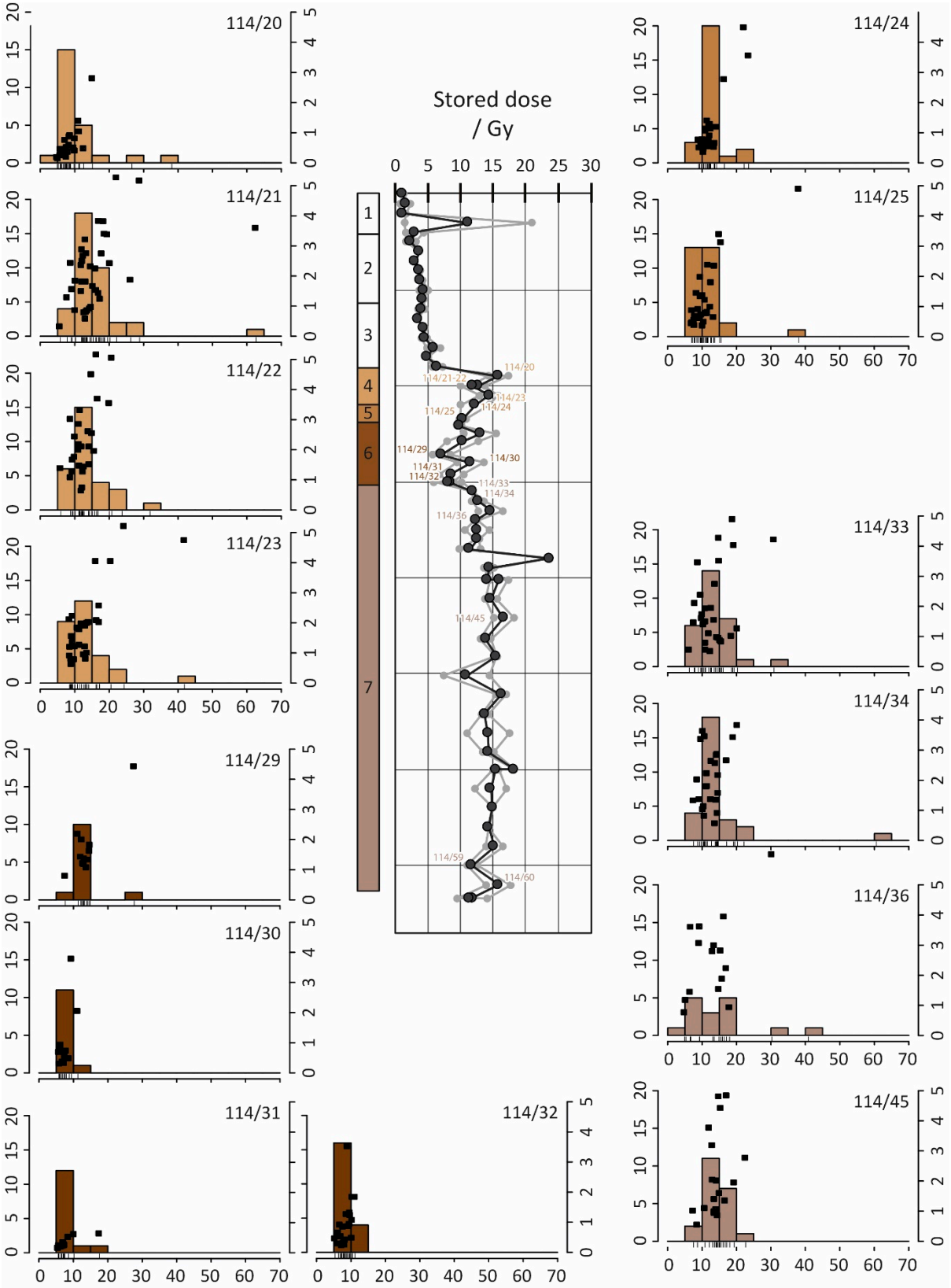

Figure S3.3: Core ELF1A, De estimates plotted vs depth in the stratigraphy, for 90-150micron quartz

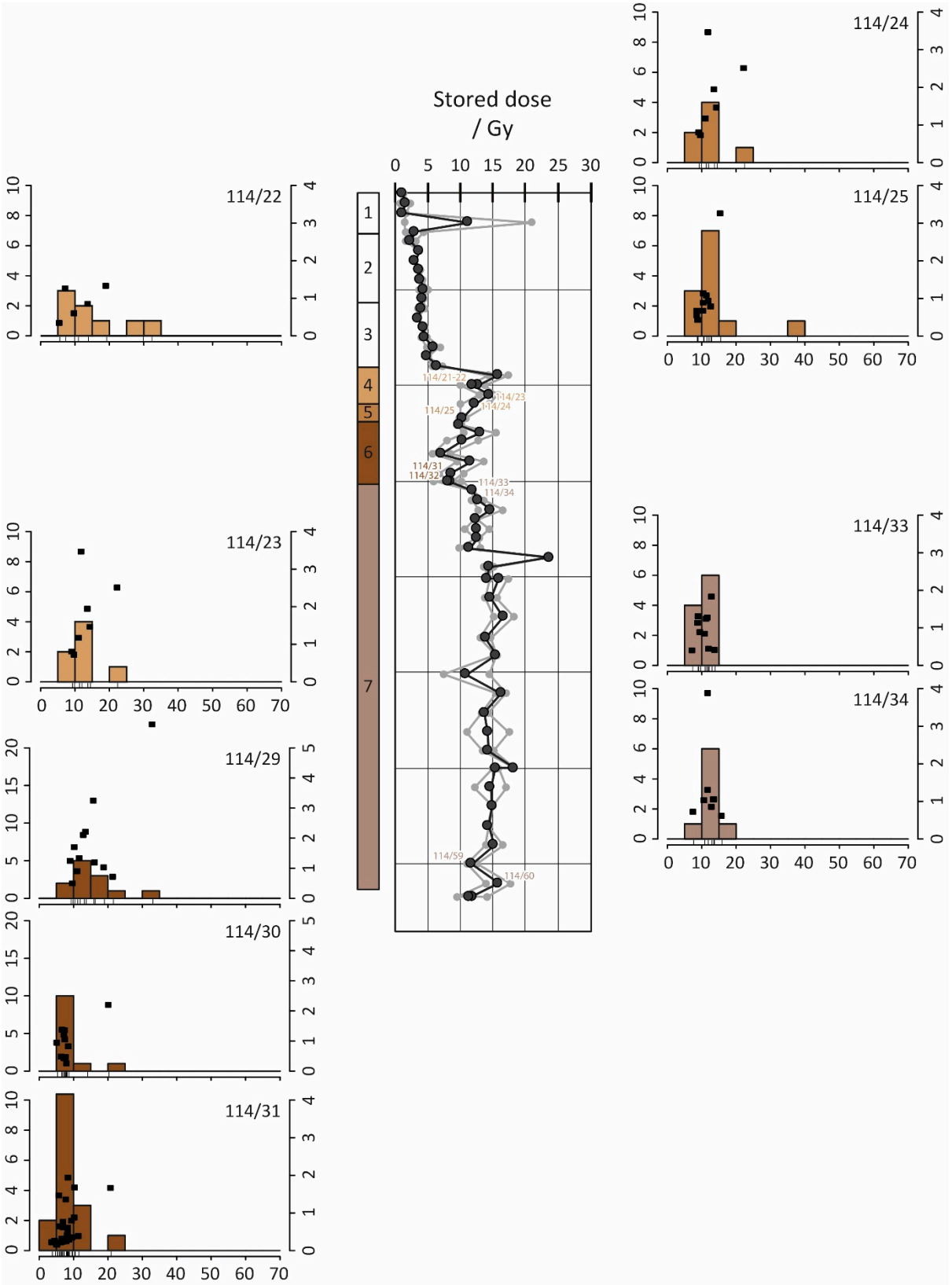
Stored dose
/ Gy
0 5 10 15 20 25 30
1
2
3
4
5
6
7
114/21-22
114/23
114/24
114/25
114/31
114/32
114/33
114/34
114/59
114/60
114/22
114/23
114/24
114/25
114/29
114/30
114/31
114/33
114/34
0 10 20 30 40 50 60 70

Figure S3.4: Core ELF1A, De estimates plotted vs depth in the stratigraphy, for 150-250micron quartz

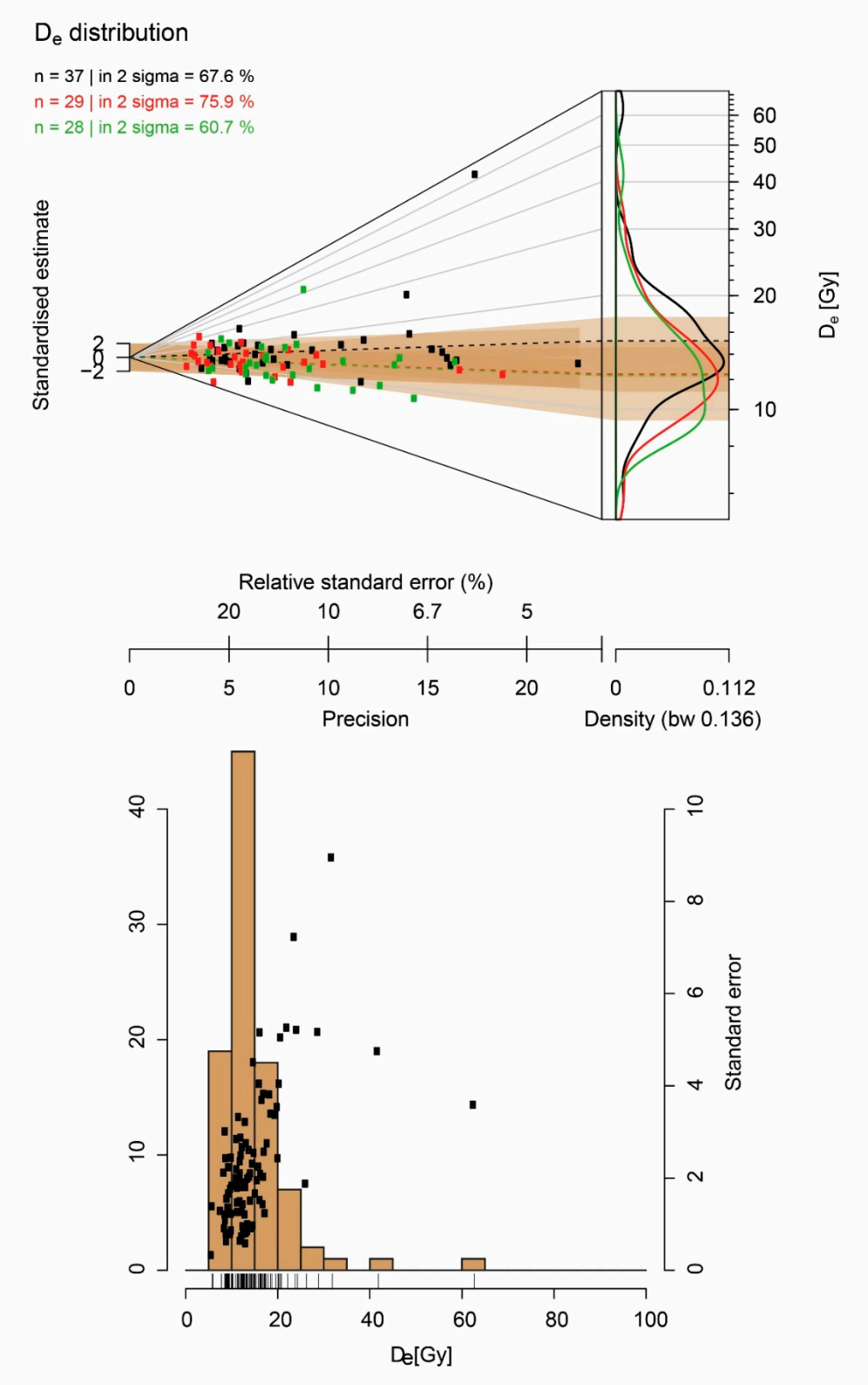

Figure S3.5: Dose distribution analysis as applied to ELF001A

Unit 4 (tidal mudflats), illustrated as an Abanico Plot and Histogram plot (generated with R luminescence package[47].

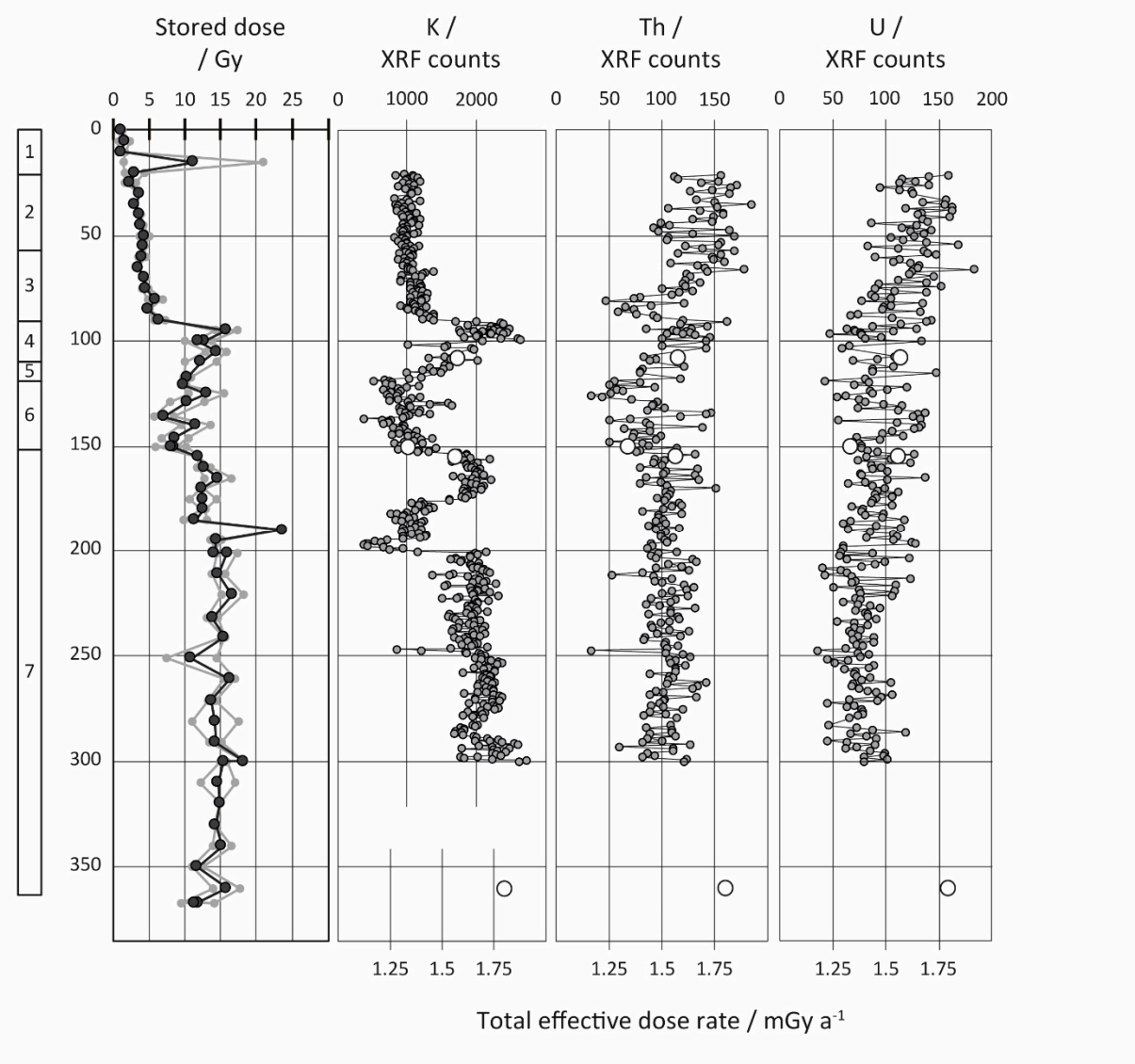

Figure S3.6: Core ELF001A, semi-quantitative element concentrations for K, U and Th

Obtained by X-ray Fluorescence using the Itrax® core scanner at Aberystwyth University.

Also shown, are the total effective dose rates as estimated from HRGS

Table S3.2: SAR quality criteria, 90-150µm quartz

Sample ID	Depth /cm	Sensitivity/ counts Gy^{-1}	Recuperation /%	Recycling ratio	IRSL response / %	Dose recovery ratio
114/20	95	5010 ± 4140	4.2 ± 1.9	1.01 ± 0.05	2.1 ± 2.6	1.00 ± 0.09
114/21	100	1180 ± 510	6.8 ± 6.9	1.05 ± 0.07	4.3 ± 11.4	1.01 ± 0.09
114/22	100	1200 ± 620	8.7 ± 5.1	1.03 ± 0.05	6.0 ± 11.3	1.01 ± 0.06
114/23	105	1360 ± 570	7.3 ± 5	1.05 ± 0.07	n/a	1.01 ± 0.06
114/24	110	2190 ± 1810	5.1 ± 2.2	1.01 ± 0.05	0.6 ± 0.8	1.02 ± 0.08
114/25	117	1610 ± 750	5.8 ± 2.7	1.01 ± 0.07	1.2 ± 1.9	1.05 ± 0.12
114/29	136	2140 ± 280	4.2 ± 1.3	0.92 ± 0.05	22.8 ± 14.6	0.97 ± 0.07
114/30	140	2120 ± 460	5 ± 3.6	1.03 ± 0.1-	11.6 ± 12.2	0.99 ± 0.08
114/31	146	5180 ± 2150	4.3 ± 1.2	1.01 ± 0.04	38.0 ± 21.5	1.07 ± 0.04
114/32	150	2800 ± 730	6.3 ± 5.2	0.98 ± 0.08	0.9 ± 1.5	1.01 ± 0.07
114/33	155	1910 ± 210	1.6 ± 1.1	0.98 ± 0.04	2.1 ± 3.7	1.00 ± 0.03
114/34	160	1770 ± 300	1.9 ± 2.4	1.00 ± 0.11	2.0 ± 2.4	0.99 ± 0.10
114/36	170	1590 ± 320	2.7 ± 2.9	1.07 ± 0.07	4.0 ± 3.0	0.94 ± 0.06
114/45	190	1850 ± 260	1.9 ± 1.6	1.02 ± 0.12	0.5 ± 0.7	1.01 ± 0.08
114/59	340	1830 ± 180	1 ± 0.7	0.97 ± 0.09	2.0 ± 1.5	0.97 ± 0.07
114/60	350	1760 ± 150	0.8 ± 0.9	1.03 ± 0.07	0.9 ± 1.0	1.05 ± 0.10
unit 4/	100-105	1310 ± 570	7.4 ± 5.1	1.04 ± 0.06	6.0 ± 11.8	1.02 ± 0.12
unit 5/	110-117	2010 ± 1350	7.2 ± 5.2	1.02 ± 0.04	0.6 ± 0.7	1.00 ± 0.05
unit 6/	136-150	3030 ± 1380	5.1 ± 3.4	0.99 ± 0.08	17.1 ± 19.8	1.02 ± 0.07

Table S3.3: SAR quality criteria, 150-250 µm quartz

Sample ID	Depth /cm	Sensitivity/ counts Gy^{-1}	Recuperation /%	Recycling ratio	IRSL response / %	Dose recovery ratio
114/20	95	n/a				
114/21	100	n/a				
114/22	100	1390 ± 810	6.3 ± 1.5	1.05 ± 0.07	0.48 ± 0.46	1.00 ± 0.08
114/23	105	2090 ± 1000	6.8 ± 6.2	1.06 ± 0.06	n/a	0.94 ± 0.01
114/24	110	3690 ± 1400	5.3 ± 2.8	1.00 ± 0.03	2.8 ± 3.1	1.02 ± 0.05
114/25	117	3260 ± 1580	3.0 ± 2.7	0.99 ± 0.05	2.3 ± 3.4	1.02 ± 0.07
114/29	136	2310 ± 500	3.4 ± 2.5	0.97 ± 0.11	17.0 ± 18.6	0.96 ± 0.09
114/30	140	2560 ± 560	8.4 ± 6.7	1.02 ± 0.06	3.6 ± 5.6	0.99 ± 0.05
114/31	146	6620 ± 5820	3.8 ± 1.3	0.98 ± 0.04	36.9 ± 23.8	1.07 ± 0.06
114/32	150	n/a				
114/33	155	2550 ± 420	3.8 ± 3.6	1.06 ± 0.05	0.62 ± 0.70	0.99 ± 0.06
114/34	160	1850 ± 360	4.1 ± 3.2	0.98 ± 0.07	1.3 ± 1.5	0.95 ± 0.10
114/36	170	n/a				
114/45	190	n/a				
114/59	340	n/a				
114/60	350	n/a				
unit 4	100-105	1740 ± 900	6.6 ± 4	1.05 ± 0.05	0.48 ± 0.46	0.97 ± 0.06
unit 5	110-117	3350 ± 1230	8.4 ± 5	1.01 ± 0.05	1.6 ± 2.4	1.00 ± 0.05
unit 6	136-150	4100 ± 2920	4.7 ± 4.3	0.97 ± 0.10	24.6 ± 24.2	1.01 ± 0.06

Table S3.4: Radionuclide concentrations as determined by HRGS, converted to dry dose rates using the conversion factors of Guérin et al. (2011)

Sample ID	HRGS

	Radionuclide concentrations [a]			Dose rates, Dry / mGy a^{-1}		
	K / %	U / ppm	Th / ppm	$\dot{D}_\alpha$	$\dot{D}_\beta$	$\dot{D}_\gamma$
ELF1A 108 cm	1.46 ± 0.12	1.65 ± 0.12	3.49 ± 0.22	7.2 ± 0.38	1.42 ± 0.09	0.72 ± 0.03
ELF1A 150 cm	1.21 ± 0.11	1.07 ± 0.1	3.83 ± 0.3	5.82 ± 0.36	1.15 ± 0.09	0.60 ± 0.03
ELF1A 155 cm	1.53 ± 0.12	1.5 ± 0.11	3.07 ± 0.2	6.45 ± 0.33	1.44 ± 0.10	0.70 ± 0.03
ELF1A 360 cm	1.86 ± 0.15	1.84 ± 0.13	3.83 ± 0.25	7.97 ± 0.41	1.75 ± 0.12	0.85 ± 0.04

Table S3.5: Radionuclide concentrations as directly measured by ICPMS

Sample ID	Equivalent to	Depth /cm	K / %	U / ppm	Th / ppm
119 [95-100]	114/20	95-100	1.75 ± 0.07	2.22 ± 0.12	8.2 ± 0.4
114/21-22 [100]	114/21-22	100	2.52 ± 0.06	3.63 ± 0.18	14.9 ± 0.8
120 [100-105]	114/21-22	100-105	1.95 ± 0.05	2.53 ± 0.09	9.1 ± 0.3
122 [110-117]	114/24-25	110-117	1.37 ± 0.05	1.84 ± 0.09	5.6 ± 0.3
114/28-29 [129-136]	114/28-29	129-136	0.81 ± 0.03	1.24 ± 0.01	4.3 ± 0.2
114/31-32 [146-150]	114/31	146-150	0.82 ± 0.02	0.88 ± 0.04	2.5 ± 0.1
114/33-34 [155-160]	114/33	155-160	2.27 ± 0.04	2.73 ± 0.08	10.5 ± 0.3
114/35-36 [165-170]	114/34	165-170	2.23 ± 0.06	2.44 ± 0.06	9.3 ± 0.3
114/44-45 [201-211]	114/40	201-211	2.24 ± 0.10	2.37 ± 0.03	8.8 ± 0.1
SdAR-L2	-	-	3.57 ± 0.18	2.04 ± 0.10	24.3 ± 1.2

Table S3.6: Environmental dose rates to HF-etched quartz, reconciled from the HRGS and ICPMS data, and attenuated for grain size and water content

Sample ID	Depth /cm	Effective beta dose rate / mGy a^{-1}	Effective gamma dose rate / mGy a^{-1}	Total effective environmental dose rate / mGy a^{-1}
114/20	95	1.30 ± 0.07	0.69 ± 0.03	2.00 ± 0.05
114/21	100	1.98 ± 0.10	0.68 ± 0.04	2.66 ± 0.08
114/22	100	1.46 ± 0.07	0.63 ± 0.04	2.09 ± 0.06
114/23	105	1.18 ± 0.11	0.57 ± 0.05	1.75 ± 0.07
114/24	110	1.02 ± 0.06	0.44 ± 0.07	1.46 ± 0.08
114/25	117	0.63 ± 0.03	0.42 ± 0.07	1.05 ± 0.07
114/29	136	0.59 ± 0.06	0.42 ± 0.07	1.01 ± 0.07
114/30	140	0.59 ± 0.06	0.42 ± 0.07	1.00 ± 0.07
114/31	146	0.57 ± 0.03	0.42 ± 0.07	0.99 ± 0.07
114/32	150	1.68 ± 0.08	0.62 ± 0.06	1.00 ± 0.13
114/33	155	1.64 ± 0.15	0.66 ± 0.05	1.65 ± 0.18

Table S3.7: Dose rates and stored doses for the 90-150 µm fraction for ELF001A

CERSA ID	Depth /cm	Unit		Dose rate / mGy a^{-1}	Stored dose / Gy
114/20	95	Unit 4, estuarine mudflats		2.00 ± 0.05	8.36 ± 0.53
114/21	100			2.66 ± 0.08	15.6 ± 1.07
114/22	100			2.09 ± 0.06	12.74 ± 0.40
114/23	105			1.75 ± 0.07	12.55 ± 0.72
114/24	110	5	Tsunami	1.46 ± 0.08	11.45 ± 0.32
114/25	117			1.05 ± 0.07	10.66 ± 0.89
114/29	136	Unit 6		1.01 ± 0.07	13.34 ± 0.99
114/30	140			1.00 ± 0.07	7.19 ± 0.31
114/31	146			0.99 ± 0.07	7.48 ± 0.66
114/32	150			1.00 ± 0.13	8.30 ± 0.35
114/33	155	7, EM - RM		1.65 ± 0.18	15.14 ± 1.81

S3.2 AMS Radiocarbon dating Radiocarbon measurements were taken on shells from molluscs recovered from 140–145 cm depth in ELF001A, 211-212cm and 314-316cm depth in ELF003, Table S3.8. The shells were submitted to Beta Analytic Inc. where they were pretreated following methods found on their website (https://www.radiocarbon.com/carbon-dating-shells.htm) and dated by accelerator mass spectrometry (AMS). Beta Analytic round all uncalibrated radiocarbon ages to the nearest 10 years, according to the Trondheim convention[48,49] and assign a conservative minimum error of ±30 ^{14}C years.

The radiocarbon age is calibrated in OxCal v4.3[50] using the internationally agreed Marine13 calibration curve of Reimer et al (2013)[51] and a local marine reservoir correction (ΔR) of −3 ±99 years, which was calculated using the 14Chrono Centre database (http://calib.org/marine/) and the 10 nearest data points to 55.1369' N, 3.4086' W.

Table S3.8 Calibrated radiocarbon dates from tsunami associated strata in cores ELF001A and ELF003

Core	Depth (m)	Laboratory number	Material	Calibration Method	Radiocarbon Age (BP)	Calibrated Age (cal BP) at 95.4%
ELF001A	1.40-1.45	Beta - 505683	Shell	Marine13	8340 +/- 30	9258 - 8935
ELF003	2.11-2.12	Beta - 493397	Shell	Marine13	8400 +/- 30	9374 - 8592
ELF003	3.14-3.16	Beta - 493399	Shell	Marine13	8350 +/- 30	9315 - 8533

References to supplementary text S3

Aitken, M. J., 1983. Dose rate data in SI units. *PACT*, **9**, p. 69–76.

Burbidge, C.I., Sanderson, D.C.W., Housley, R.A. and Jones, P.A., 2007. Survey of palaeolithic sites by luminescence profiling, a case study form Eastern Europe. *Quaternary Geochronology*, **2**, p. 296–302.

Dietze, M., Kreutzer, S., Fuchs, M. C., Burow, C., Fischer, M. and Schmidt, C., 2013. A practical guide to the R package Luminescence. *Ancient TL*, **32**, p. 11-18.

Guérin, G., Mercier, N. and Adamiec, G., 2011. Dose-rate conversion factors: update. *Ancient TL*, **29**, p. 5-8.

Guérin, G., Christophe, C., Philippe, A., Murray, A. S., Thomsen, K. J., Tribolo, C., Urbanova, P., Jain, M., Guibert, P., Mercier, N., Kreutzer, S., and Lahaye, C., 2017. Absorbed dose, equivalent dose, measured dose rates, and implications for OSL age estimates: Introducing the Average Dose Model: *Quaternary Geochronology*, **41**, p. 163-173.

Kinnaird, T.C. and Bates, M., 2018. Characterising the luminescence stratigraphies of cores ELF1A and ELF19, Europe's Lost Frontiers. *CERSA Luminescence Report, University of St Andrews*

Kinnaird, T. C., Dawson, T., Sanderson, D. C. W., Hamilton, D., Cresswell, A. and Rennel, R., 2017. Chronostratigraphy of an eroding complex Atlantic round house, Baile Sear, Scotland. *Journal of Coastal and Island Archaeology*, published online.

Mejdahl, V., 1979. Thermoluminescence dating: Beta-dose attenuation in quartz grains. *Archeometry*, **29**(1), p. 61-72.

Murray, A. S. and Wintle, A. G., 2000. Luminescence dating of quartz using an improved single-aliquot regenerative-dose protocol. *Radiation Measurements*, **32**(1), p. 57-73.

Prescott, J. R., and Hutton, J. T., 1994. Cosmic ray contributions to dose rates for luminescence and ESR dating: Large depths and long-term time variations. *Radiation Measurements*, **23**(2), p. 497-500.

Sanderson, D.C.W., Bishop, P., Stark, M.T. and Spencer, J.Q., 2003. Luminescence dating of anthropogenically reset canal sediments from Angkor Borei, Mekong Delta, Cambodia. *Quaternary Science Reviews*, **22**, p. 1111-1121.

Sanderson, D.C.W. and Murphy, S., 2010. Using simple portable OSL measurements and laboratory characterisation to help understand complex and heterogeneous sediment sequences for luminescence dating. *Quaternary Geochronology*, **5** (2), p. 299-305.

Supplementary Text 4 Palaeoenvironmental proxy analyses

S4.1 Foraminifera and ostracods

A rapid assessment of the samples was undertaken on 15 samples. A range of materials were present in the samples including plant debris and seeds, molluscs, diatoms, and insect remains. Foraminifera and ostracods were present in all samples.

Three microfossil facies associations have been identified from the samples (Table S4.1). The lowermost facies (associated with unit ELF001A-7) appears to be one indicative of estuarine mudflats. The microfaunas are very restricted (suggesting brackish conditions). The foraminifera are often very small and the ostracods are represented invariably by small juveniles. This is odd and may be, in part, a function of reduced salinities in the environment. This lower part of the sequence also contains the remains of many spirorbid polychaete worms, which are normally attached either to a hard substrate or seaweed. In the absence of a hard substrate it is likely that seaweed was common and this suggests an abundance of algae on the mudflats. There are also a few juvenile molluscs in this part of the sequence. The "marine" component is also limited and therefore suggests the site is open to the estuary or part of a gulf (with reduced salinities). The basal sample also contains rare *Jadammina macrescens* which is a high saltmarsh foraminifer and may be indicative of saltmarsh in the vicinity of the sampling site at this time. Its disappearance above 3.67m may suggest waning saltmarsh conditions.

The second facies type is associated with the coarser sediments of units EF001A-5 and ELF001A-6 that contains both brackish hydrobids and marine oyster shells. These remains are very fragmentary and typically smashed. The ostracods, especially the brackish component, also exhibits damage with many valves broken. This part of the sequence

contains a greater number of outer estuarine and marine forams alongside the tidal mudflat and estuarine foraminifera and ostracods noted below. Unit EF001A-5 also contains a few agglutinating foraminifera of high saltmarsh (*Trochimmina inflata* and *Jadammina macrescens*).

The third facies type is associated with unit ELF001A-4 and is dominated by estuarine mudflat species. By comparison with the lower mudflat facies this association appears to be indicative of more open estuarine conditions evidenced by more diverse microfaunas especially of adult brackish ostracods and a greater outer estuarine marine component in general.

Ecology	Estuarine mudflats	Storm surge or tsunami deposit. Contains stones (some exotic), both marine and brackish molluscs and microfauna (often broken/fragmentary)							Estuarine mudflats with some algae (and attached fauna)							
DEPTH IN CORE	0.96-0.97m	1.03-1.04m	1.10-1.11m	1.15-1.16m	1.20-1.21m	1.30-1.31m	1.35-1.37m	1.47-1.48m	1.66-1.67m	2.10-2.11m	2.46-2.47m	2.80-2.81m	3.09-3.10m	3.47-3.48m	3.67-3.68m	
DEPTH (O.D.)																
Lithological units	1A-4		1A-5		1A-6						1A-7					
BRACKISH FORAMINIFERA																
Ammonia(brackish sp.)	xxx	xxx	xxx	xxx	xx	xx	xxx	xxx	xxx	xx	xx	xx	xx	xxx	xxx	calcareous foraminifera of tidal mudflats
Haynesina germanica	x	x	x	x	o	o	x	x	xx	x	x	x	x	xx	xx	
Elphidium williamsoni	x	xx	x	x	x	x	x	x	x				o	x	x	
Quinqueloculina(brackish sp.)									o					x	x	
Trochammina inflata			o												o	agglutinating forams of high saltmarsh
Jadammina macrescens			x													
OUTER ESTUARINE/MARINE FORAMINIFERA																
Ammonia tatavus	x	x	xx	x	x	x	x	x	xx	xx	xx	xx	xx	xxx	xxx	essentially marine foraminifera, but can penetrate open estuaries
miliolids	x	xx	xx	o	o	o	xx	x	xx	xx	xx	x		o	xx	
lagenids		xx	o	x	o										x	
Elphidium macellum				x		o	o									
BRACKISH OSTRACODS																
Loxoconcha elliptica	x	xx		x	x	x	x	x	x	x	x	x	x	x	x	brackish ostracods of estuarine mudflats
Cyprideis littoralis		xx							o		x	x				
Cyprideis torosa		x	o	x	x	o	x	x	xx	o	x	o		x	x	
Leptocythere porcellanea		x		x			xx	xx	x	x	x		o	x	x	
Cytheromorpha fuscata		o														
Leptocythere castanea					o				x	o	o			x		
Cytheros fischeri																
OUTER ESTUARINE/MARINE OSTRACODS																
Hirschmannia viridis	x		x	x	o			xx	x	x	x	x	x	x	xx	essentially marine ostracods, but can penetrate open estuaries
Robertsonites tuberculatus	x	x		o	o			x								
Palmocythere guttata	o	xx	x			o									x	
Hemicythere villosa		x		x	x	x	xx	xx								
Cytheropteron latissimum		x											x	x		
Semicytherura nigrescens		x	o													
Palmocythere laevata		o		x				x								

Foraminifera and ostracods are recorded: o – one specimen; x – several specimens; xx – common; xxx – abundant

e.g. 0.96-0.97m: samples received 7/1/2017
e.g. 1.10-1.11m: samples received 21/1/2017

Table S4.1 Foraminifera and ostracod abundance profiles of core ELF001A.

S4.2 Pollen analysis: Subsamples of 1cm^3 were extracted from the core at 0.05m intervals and prepared for pollen analysis using standard methodologies, including HF treatment and Acetylation. *Lycopodium* spores were added to permit the calculation of pollen concentrations. Pollen counting was carried out on a Leica DM100 at a magnification of x400. All pollen nomenclature follows Moore *et al.* (1991)[52] with the amendments proposed by Bennett *et al.* (1994)[53]. At least 150 pollen grains were counted per sample.

The results are presented as a pollen diagram produced using TILIA and TILIA*GRAPH[54] (Figure 4, Figure S4.1A). Microscopic charcoal fragments were counted and are expressed as a percentage of total land pollen. The diagram has not been divided into biostratigraphic assemblage zones, but the position of the *Tsunami* deposit between 1.03-1.55m is indicated, dividing the sequence into pre- and post-*Storegga*; no pollen was preserved in this unit (Unit ELF001A-6). The diagram is dominated by relatively few, predominantly arboreal taxa: total tree and shrub percentages are generally above 90% total land pollen (TLP) with herbs accounting for a maximum of 20%. This implies the presence of dense woodland in the pollen source area. *Corylus avellana*-type (likely to be hazel, rather than *Myrica gale* in this situation), is dominant throughout (c. 60% TLP). Other trees which are consistently recorded but at lower percentages, are *Quercus* (oak) and *Pinus sylvestris* (Scots' pine) (both c. 10-20%), with lower values for *Ulmus* (elm; up to 5%), *Alnus glutinosa* (black alder; c. 5%) and *Betula* (birch, max 9%). Other trees/shrubs recorded sporadically at low percentages are *Tilia* (lime), *Salix* (willow), *Fraxinus* (ash) *Hedera helix* (ivy) and *Ilex aquifolium* (holly). Herbaceous taxa account for a relatively low proportion throughout, but with Poaceae (wild grasses) consistently present (max 15%). Another herb recorded in almost every sample (max 5%) is *Silene dioica*-type (red campion), whilst Cyperaceae (sedges), Chenopodiaceae (Fat Hen family), *Artemisia*-type (mugwort). Ranunculaceae

(buttercups), *Filipendula* (meadowsweet) and a few other herbs make occasional appearances including *Sedum* (stonecrop). Spores including Pteropsida (monolete) indet. (ferns), *Polypodium vulgare* (common polypody), *Sphagnum* (bogmoss) and *Pteridium aquilinum* (bracken) are present throughout, with the former best represented (max 8% TLP+spores). Proportions of microscopic charcoal are rather variable, but seem to be higher in the uppermost three samples of the sequence. The spectra are remarkably consistent, other than for a spike in *Quercus* at 2.65m, associated with a reduction in *Corylus*. It is difficult to assess what processes this temporary expansion of oak relates to as there are no other pronounced changes at this level.

Overall, the sequence indicates a landscape of deciduous woodland, in which hazel was dominant with oak, pine, elm and birch as subordinate components, and alder and willow on damper soils. The impression of a shady, closed woodland is reinforced by the presence of ivy and common polypody, often found as an epiphyte on oak trees. The consistent record of grass throughout may reflect the presence of open areas within the woodland, but more probably reflects the presence of wetland grasses such as *Phragmites* (reeds) growing in the lagoonal environment. The range of herbs also indicate communities typical of damp soils (buttercups, sedges, meadowsweet), perhaps growing on the ecotonal areas between the lagoon and the dryland. In particular, the consistent presence of *Silene dioica*-type is notable; the probable species represented is *Silene dioica* which typically grows in partially shaded habitats, also indicated by the record of fern spores. The Chenopodiaceae includes many herbs, but in this context is most likely to indicate plants of this family that grow on salt marshes and other saline soils; the rare records of stonecrop perhaps also reflect drier, sandy soils typical of the coast. The presence of *Pteridium* might also imply better drained

soils in the wider landscape where bracken would be found. In general there is no evidence for any form of disturbance to the environment for the duration of the record.

The most striking aspect of the sequence is the relative lack of fluctuation throughout, the curves of all the taxa are remarkably stable. Two comments are pertinent to how this relative homogeneity might be interpreted. Firstly, the data indicate that the vegetation within the pollen source area was broadly stable across the period of time represented by the diagram with no palynologically identifiable changes. Secondly, it is possible that this apparent stability of the environment through time, is related to the nature of the pollen source area for the silt dominated deposits that constitute the sequence. It is likely the pollen derived from a relatively large spatial area, including the dryland landscape adjacent to the lagoon but also terrestrial locations further upstream. In other words, the pollen record is resolving an area of landscape of potentially tens of square kilometres. Moreover, there is likely to have been a degree of mixing and reworking of the pollen within the water column, so interpretation must of necessity be tentative in terms of the extent or character of inferred vegetation dynamics throughout the sequence.

There are no pronounced changes in the spectra immediately above the hypothesised *Tsunami* layer, which might be taken to imply that this event had no identifiable impact on the local vegetation, with a predominantly wooded landscape both pre and post-*Tsunami*. However, this interpretation must be tempered by the previous comments concerning the potential taphonomic complexity of the pollen record. However, there is evidence of potential changing woodland dynamics above this unit, towards the top of the diagram, between 1.03-0.84m. Total tree pollen percentages increase as a result of rising values for *Pinus* alongside reductions in *Corylus*. Again, this is difficult to interpret but may indicate an expansion in Scots pine, prior to the establishment of marine conditions at this location.

Interestingly, there are also increased representation of microscopic charcoal across the same levels. It would be tempting to interpret these changes as potential evidence for increased dryness in the period before the final marine incursion at this location. Otherwise, there is no palynological evidence for woodland recession that would be expected to result from rising water tables in advance of rising relative sea levels.

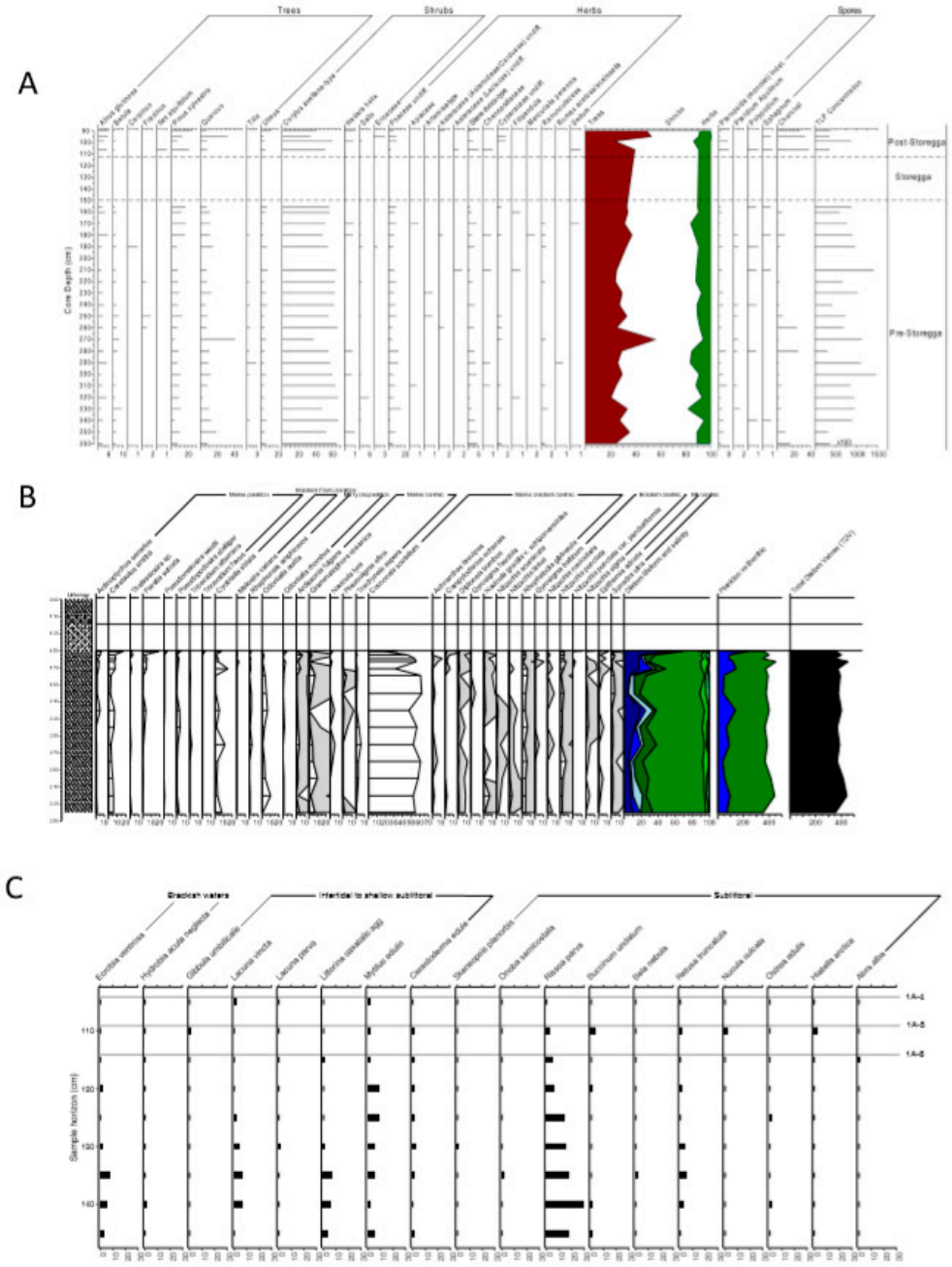

Figure S4.1 ELF001A palaeoenvironmental proxy count profiles.
All measurements taken from lithological Unit ELF001A-4 and below. A. pollen counts B. diatom counts C. mollusc counts.

S4.3 Diatom analysis*:* A selection of 23 spot samples were prepared for initial diatom assessment from the sedimentary sequence of core ELF001A. Diatom preparation followed the methodology of Plater et al. (2000)[55], with additional pretreatment using sodium hexametaphosphate, to assist in minerogenic deflocculation. Samples were sieved using a 10μm mesh to remove fine minerogenic sediments. The residue was transferred to a plastic vial, from which a slide was prepared, using Naphrax as the slide mountant, for subsequent assessment.

For samples in which diatoms were encountered in sufficient abundance during the initial assessment, a minimum of 300 diatoms were identified for each sample depth. If preservation was found to be poor, a complete slide was traversed in an attempt to extract the diatom data available from the sample under assessment. Poor preservation was experienced in the majority of samples from within and above the event stratum. Diatom species were identified with reference to van der Werff and Huls (1958-74)[56], Hendy (1964)[57] and Krammer & Lange-Bertalot (1986-1991)[58]. Ecological classifications for the observed taxa were then achieved with reference to Vos and deWolf (1988; 1993)[59,60], Van Dam et al., (1994)[61] and Denys (1991-92; 1994)[62,63].

The overall diatom signal from within the sediments underlying the event stratum can be interpreted as indicating coastal conditions prevailing throughout its depositional history (Figure 4, Figure S4.1B). The dominance of marine to brackish benthic taxa, with a particular presence of taxa often associated with plants and muddy substrates (epiphytic and epipelic taxa respectively), would infer deposition took place within the intertidal zone. The absence of aerophilous taxa and epipsammic taxa is also noted, whilst planktonic/tychoplanktonic

taxa rarely contribute more than 20-30% Total Diatom Valves (TDV) to the floral assemblages. The diatom assemblages are also found to be consistent throughout the sedimentary unit, which suggests similar conditions prevailed throughout the deposition of the sedimentary unit.

The dominant taxa, *Cocconeis scutellum,* is a 'northern' epiphytic species often encountered in the littoral zone of the North Sea and Arctic oceans[64], and is affiliated with taxa such as *Zostera marina* or seagrass (Main & McIntyre, 1974; cited in Werner, 1977)[65] as well as green algae such as Cladophora sp.[66]. Studies by Tanaka (1986)[67] have also shown that *C. scutellum* is commonly associated with seaweed (including *Sargassum horneri*, *S. patens*, *S. piluriferum*) and *Undaria* (kelp). When combined with the relative dominance of other epiphytic taxa throughout the sedimentary profile, we can first infer that deposition relatively high on the tidal frame. The low but persistent presence of marine planktonic and tychoplanktonic species indicates tidal inundations occurred, but were somewhat restricted, during the development of the deposits underlying the event stratum.

When comparing such floral assemblages encountered beneath the event stratum to the ecological groupings stipulated by Vos and deWolf (1993)[60], deposition within a setting which experiences a large tidal range is discounted. This is due to the absence of any aerophilous and epipsammic taxa, the relative dominance of marine-brackish epiphytic taxa and the relatively limited influence of planktonic and tychoplanktonic taxa. A microtidal palaeoenvironment such as a tidal lagoon or small tidal inlet is interpreted. All samples contain diatoms typical of such a depositional setting, to infer the environment remained

stable throughout the deposition of the finely laminated silt and clays that underlie the event stratum.

S4.4 Mollusca analysis: Nomenclature followed WoRMS (WORMS EDITORIAL TEAM 2018)[68]. Identifications were carried out using a reference collection. Ecological information is derived from Graham (1971)[69] and Allcock et al. (2017)[70]. Minimum number of individuals (MNI) for gastropods was determined by counting all non-repeating elements of that species within a sample and using the largest number as the MNI. In the case of bivalves, only shell hinge fragments or intact valves were counted. Minimum numbers of left and right valves are presented separately. The highest of these two numbers is used as the MNI.

Preservation was largely good in all samples, although *Mytilus* shells and other bivalves were almost invariably broken (Figure S4.1C). Numbers of shells were generally low, although shells are more frequent within Unit ELF001A-6. Numbers decline through time. At the bottom of the sequence, in Unit ELF001A-6, there is an ecologically mixed assemblage. There is a brackish water fauna present in this unit as well, represented by moderate numbers of *Ecrobia ventrosa,* and a single *Hydrobia acuta neglecta.* These are snails associated with relatively low salinities, in sheltered locations such as estuaries and lagoons, away from high energy tidal influence.. The same samples also contain low numbers of fruits of *Potamogeton spp.* (pondweed), which is found in fresh to brackish water settings. The unit is dominated, however, by taxa from a lower shore or sublittoral environment, especially *Rissoa parva.* This is a common snail under stones and on weeds from mid tidal level down to 15m depth on rocky shores. Other molluscs present in this unit include *Retusa obtusata,* a predatory gastropod which was most likely preying on *Rissoa;* and the common

mussel *Mytilus edulis,* which is usually found intertidally on rocky coasts. The mussel shells are all broken, which may suggest compression from overlying sediment or wave transport, however they are not especially rounded, which suggests they were not subjected to much wave rolling. Rather than rocky shores, common cockle, *Cerastoderma edule,* and European oyster, *Ostrea edulis,* are found in muddy and sandy environments. The intertidal to lower shore assemblage continues to dominate in Unit ELF001 A-5, however the brackish water fauna is now absent. There is lower species diversity in this unit, however there is somewhat more equitability, with *Rissoa* less dominant. In unit ELF001A-4, numbers are very low, containing just a single shell each of *Lacuna vincta* and *Mytilus edulis,* which appear to reflect an intertidal setting on a high-energy coast. Overall, the samples appear to suggest inundation of a previously low energy tidal-dominated estuarine setting and establishment of a much higher energy wave-dominated environment. The transition is not clear however, and ecological signals remain mixed throughout Unit ELF001A-6, indeed the brackish water fauna peaks at 1.35- 1.40m depth. A likely scenario is that this deposit represents a conflation of material eroded and reworked from markedly different locales (rocky, wave-dominated; and muddy, tidally-dominated). The complete absence of abrasion on the shells suggests that they were not subject to usual wave transport. Bivalve shells with angular breaks that have not been wave-rounded may be features of tsunami deposits[71], however in these samples there are no articulated bivalves, which Donato et al. also found in a recent tsunami deposit from Oman

S4.5 SedaDNA analysis

DNA extraction All DNA handling stages prior to PCR took place in a dedicated aDNA facility at the University of Warwick following standard protocols for processing ancient DNA[72].

Sealed sediment cores were refrigerated at 4°C immediately after retrieval and were held at a constant 4°C until sampling. Cores were split under strict aDNA lab conditions and under red-light to preserve samples for OSL analysis. All samples for aDNA work were taken inside a category two biosafety cabinet using sterile equipment. The cut surface of the core was removed and ~20 g of sediment retrieved, ensuring that no sediment from the outer 1 cm of the core was collected, as this may have been disturbed during the coring process. For DNA extraction, library preparation, sequencing, and downstream analysis, each sample was processed in duplicate. For each duplicate, 2 g (±0.05 g) of sediment was taken from each sample. Subsamples were processed in batches of up to seven plus one negative control (reagents only). The subsamples were mixed with 5 ml CTAB buffer (2% w/v CTAB, 1% w/v PVP, 0.1 M Tris pH 8.0, 20 mM EDTA, 1.4 M NaCl) and incubated at 37°C with agitation for 7 days. After incubation, the subsamples were centrifuged at 20,000 xg for 10 minutes. The supernatant was moved to a new 50 ml tube and manually shaken with 4 ml chloroform:isoamyl alcohol (24:1) for 5 minutes. The resulting mixture was centrifuged at 20,000 xg for 5 minutes. The aqueous phase was combined with 20 ml Buffer AW1 (Qiagen) and incubated at room temperature for 1 hour. This was then applied to silica-based spin columns using a vacuum manifold. The columns were then washed, first with 500 µl Buffer AW2 (Qiagen), and then 300 µl acetone, both followed by centrifugation at 6,000 xg for 1 minute. The columns were then removed from their collection tubes and air dried for 5 minutes. Finally, DNA was eluted in 65 or 75 µl Buffer EB (Qiagen). They were incubated at 37°C for 10 minutes and centrifuged at 15,000 xg for 2 minutes. The eluted DNA was quantified using a high-sensitivity Qubit assay (Invitrogen).

Sequence generation The library protocol is based on Meyer and Kircher (2010)[73] with the following modifications from Kircher et al. (2012)[74]: 0.1 µl of adapter mix during adapter ligation instead of 1 µl; spin column purification (MinElute PCR purification kit, Qiagen) instead of SPRI; purification step after adapter fill-in replaced with heat inactivation for 20 minutes at 80 °C; Double indexing; no fragmentation step, as ancient DNA is expected to already be shorter than 400 bp; blunt-end repair reaction volume of 40 µl; T4 DNA ligase added to individual sample tubes instead of the master mix during adapter ligation; Platinum Pfx was used indexing PCR for most samples, but since this was discontinued in 2018, Platinum SuperFi was used for some samples; there were 16 PCR cycles for most samples, but where Platinum SuperFi was used 18 PCR cycles were applied.

Libraries were visualised on a 2% agarose gel. They were then cleaned using 45 µl SPRI beads and eluted in 20 µl TET buffer[75]. The cleaned libraries were quantified using a Qubit assay (Invitrogen) and a fragment size profile produced using a Bioanalyzer (Agilent). Libraries were normalised to 4nM and pooled prior to sequencing on the Illumina NextSeq platform using the high-output, v2, 150-cycle kit (75x75 paired end), Table S4.2. Sequence data were deposited in the European Molecular Biology Laboratory European Bioinformatics Institute (project code PRJEB33717).

Bioinformatics Raw BCL files were converted to FASTQ and demultiplexed using Illumina's bcl2fastq software (version v2.20.0.422), using the --no-lane-splitting and --ignore-missing-bcl options. Adapters were removed and paired end reads were collapsed using AdapterRemoval (version 2.2.2)[76], specifying a minimum length of 30 and a minimum quality of 30. FastQC (version 0.11.6)[77] was used to visually assess the success of adapter

and quality trimming. FASTQ reads were converted into FASTA format using the following example shell command: In.fastq | awk 'NR%4 !=0' | awk 'NR%3 !=0' | sed 's/@/>/g' > out.fasta. Finally, duplicates were removed using the fastx_collapser command from the FASTX-toolkit (version 0.0.13)[78].

An initial metagenomic BLASTn search (version 2.6.0)[79] was undertaken using the tab output (specified using -outfmt "6 std staxids"). This allows a large volume of data to be processed with a far smaller data footprint than the full BLAST output format. This was then converted to RMA format using the MEGAN5 command line (version 5.11.3)[80], enabling the visualisation of the preliminary data. The patchiness of DNA sequence databases and the overrepresentation of model organisms leads to unreliable assignation of sequences. Reads were therefore stringently filtered using the Phylogenetic Intersection Analysis (PIA)[81]. FASTA sequence reads with preliminary assignation to taxa of interest (in this case Viridiplantae, Chordata with primate reads excluded, Arthropoda, and a random subset of 10,000 bacterial reads) were extracted from the RMA files using MEGAN5 command line tools (version 5.11.3)[80], These reads were subjected to a second round of BLASTn (version 2.6.0)[79], this time to generate the full BLAST format as an output. These were then used as an input for Phylogenetic Intersection Analysis (Smith et al., 2015; default settings) [81] in order to retrieve stringent assignations. Taxa with >2% of the assigned reads also assigned to that taxon in the negative controls for that sequencing run were removed. Any taxa that remained after the stringent filtering that were not native to Europe were discarded, accounting for about 3% of the data.

Authentication: DNA damage analysis Two approaches were taken to establish whether damage patterns characteristic of ancient DNA were present to authenticate the sedaDNA. Current damage authentication methodology is predicated on the reconstruction of ancient genomes[16], rather than metagenomic assemblages present in shotgun data where the coverage of any one genome may be too low for a significant signal. Fortunately, a number of tree species from the Unit ELF001A-6 were well enough represented to use this approach, *Quercus*, *Betula* and *Corylus*. Paired end collapsed reads were mapped to *Betula*, *Corylus*, and *Quercus* genomes (accessions: GCA_900184695.1, C.avellana_Jefferson OSU 703.007, and GCA_900291515.1 respectively) using BWA-ALN (version 0.7.12-r1039)[82] specifying -n as 0.01 and -l as 1000. BAM files were generated using bwa samse (version 0.7.12-r1039)[76xx], and samtools view with the -Sb flag (version 1.7) [83]. Read group tags were added using picard AddOrReplaceReadGroups (version 2.18.7) (http://broadinstitute.github.io/picard/), then duplicates were marked and removed using picard MarkDuplicates. Realignment around indels was undertaken using the GATK tools RealignerTargetCreator and IndelRealigner (GATK version v3.8-1-0-gf15c1c3ef) [84]. All intermediary sorting and indexing stages were undertaken using the samtools sort and index tools (version 1.7) [83]. MapDamage (version 2.0.6)[16] was then used to assess the extent of DNA damage patterns using the –merge-reference-sequences option. Fragment misincorporation plots can be seen in Figure S4.2. The fragmentation parameter was calculated for these genome mapped data sets using the methodology of Kistler *et al.* 2017[15], Figure S4.3.

A second novel methodology was also applied which does not require mapping DNA to a genome to estimate misincorporation parameters, to allow the assessment of a

taxonomically mixed assemblage. The metagenomic damage analysis tools allows for the assessment of post-mortem deamination patterns on a metagenomic scale (i.e. whole sequence sample files), instead of an individual reference genome comparison with individual hits, used with tools such as MapDamage[16]. Metagenomic damage analysis is based on a three-step bioinformatic process, and examines the first 5' 19 base pair positions. All sequences were subjected to metagenomic BLASTn analysis[79] with the 'qlen' option, using the full NCBI nt database. The 'qlen' option creates a standard output with the known available positions and the full sequence length for each hit. Using the BLAST outputs, a combined fasta file of the hit IDs and associated reference genome sequence was then created using Efetch (part of the Enterez direct tool) within the E-Utilities package, which provides access to the NCBI's suite of interconnected databases. This process was piped into PERL script 'Efetch.pl', which is a four-step process. The script firstly opens the BLAST output and, on a conditional argument, builds in a directional variable which sorts the base-pair start and end position depending on whether the read is in non-reversed or reverse complemented alignment. Once the start and end coordinate of each hit is sorted, the script using the efetch command, connects to the NCBI database and copies the associated organism information and positional read from the reference genome. If in the reverse complement, the next step is to reverse it to the original sequence alignment. Finally, the hit ID, organism information and the matched section of the reference genome are piped into individual FASTA files for each of the original BLAST ID hits. Once each individual FASTA file is created, using PERL script 'newBlastParse.pl', the sequence from each hit from the original BLAST output was then appended to the associated individual FASTA file, creating a two record FASTA. This process finds the query ID, subject ID and the sequence from the original BLAST output, and prints into the associated FASTA file created

in the previous step. Once a fully populated FASTA file for each individual BLAST hit was created, the Efetch record and the BLAST ID were realigned using the Needleman-Wunsch algorithm[85], using the 'aln.pl' which records the alignment of each base pair. Once aligned, each hit was assessed for positional mismatches using PERL script 'mismatches.pl', which examines each base position and counts the prevalence of any C > T misincorporations. The positional mismatches were visualised in RStudio (V1.1.456).

The constant 4˚C environment of the sea floor leads to an expectation of damage which may be as low as 2.5% of terminal overhang cytosines deaminated in the age ranges explored in this study[15], which may be below levels of detectability as has been observed in previous studies[81,86]. Furthermore, the high ionic environment of marine conditions is expected to reduce deamination rates by reducing the rate of hydrolytic attack[87,88], as has been observed for marine environments[89,90]. Here we observed deamination rates in the range of 7-15% which is in line with these expectations of low damage levels for the sediments of Unit ELF001A-6, OSL dated to 8.14 ± 0.29 ka (Figure S4.2).

The metadamage analysis across the sedaDNA set confirms this low level of damage signal, agreeing closely with the mapdamage assessment indicating damage levels are reflected across taxa (Figure S4.4). We applied the metadamage analysis to sequence data both before and after the PIA filtration step. The mismatch base line in the post PIA analysis data is lower than the pre-filtered data, indicating a lower level of phylogenetic background noise as would be expected as less accurate phylogenetic assignations are rejected. In this way the metadamage analysis validates the PIA analysis.

Fragmentation profiles indicate a high variance within horizons indicating poor correlation with age as has previously been observed[15] (Figure S4.3).

Biogenomic mass Shotgun data have the potentially useful property of representing the biomass of organisms present in terms of cell counts, if genome size is taken into account. We used C values of the Kew Angiosperm database (http://www.kew.org/cvalues/) to estimate representative genome sizes for floral taxonomic units, while we used the Animal Genome Database (http://www.genomesize.com) for faunal estimates. We calculate a biogenomic mass value by dividing the number of sequence read counts observed for a taxon by the genome size to give a counts per gigabase value. This value should give an estimate that is directly proportional to the number of cells left behind by organisms, assuming minimal effects of clonal bias in library preparation, Figure 4. Both raw count values and associated biogenomic mass values are represented for floral (Figure S4.5) and faunal (Figure S4.6) for core ELF001A, and values for floral profiles are shown for cores ELF003, ELF0031A, ELF0039 and ELF059A (Figure S4.7).

Authentication: stratification analysis: Studies of sedaDNA need to establish the stratigraphic integrity of ancient DNA recovered, and whether there has been post deposition movement of DNA up and down the sediment column as has been observed in past studies[91]. To date, no clear methodologies have been established for best practice to check for DNA movement. Here we applied a statistical approach to calculate the probability that taxon counts between horizons could have been drawn from the same statistical distribution, indicating homogeneity of DNA titre across horizons and therefore complete diffusion. While complete diffusion represents the extreme of DNA movement, the

probability never the less provides a metric of the abruptness of change allowing an evaluation of the likelihood horizon pairs are part of the same diffused population. The methodology is equally applicable to other biological proxy data such as pollen and diatoms, and so was applied to the data sources in this study. Taxon counts are assumed to follow a Binomial distribution where the total count number represents the trial number, and the taxa count is the number of observed successful outcomes. We then applied Beta distributions to explore the underlying probability of the Binomial distributions where parameters a and b were derived from the number of counts of a taxon and the total number of counts minus the taxon counts respectively. The probability that two sets of taxon counts were derived from the same underlying distribution (*p value*) was inferred from the area of overlap between the two derived Beta distribution probability density functions (Figure 4, Figure S4.8).

We further quantified the extent of change in taxon count number between by applying an index of change (Figure 4, Figure S4.5) outlined in equations 1 and 2:

$$Change\ Index = \frac{(a-b)}{b} \times 100\ where\ a > b \qquad (1)$$

$$Change\ Index = \frac{(b-a)}{a} \times -100\ where\ b > a \qquad (2)$$

Where a and b are the maximum likelihood estimators of the probability of a count being assigned to a particular taxon as derived from the Beta distribution of the overlying and underlying horizons respectively.

Highly significant differences were observed between horizons, indicating a lack of movement of DNA in the sediment column. In the case of Unit ELF001A-6 and the underlying Unit ELF001A-7, *p* values for woody taxa such as Fagales (9.9×10^{-51}), Quercus (5.2×10^{-5}), Betula (5.96×10^{-25}), Saliliceae (7.63×10^{-57}) and the Amygdaloideae (1.17×10^{-257}) are highly convincing of an abrupt change and therefore lack of DNA movement, Figure 4. Note in the case of ELF003 radio carbon dates indicate an inversion in which the underlying tsunami associated unit is younger than the overlying units, hence the significant fall in tree taxa comparing these two units (Figure S4.8) should be interpreted as a significant influx of woody taxa associated with the tsunami.

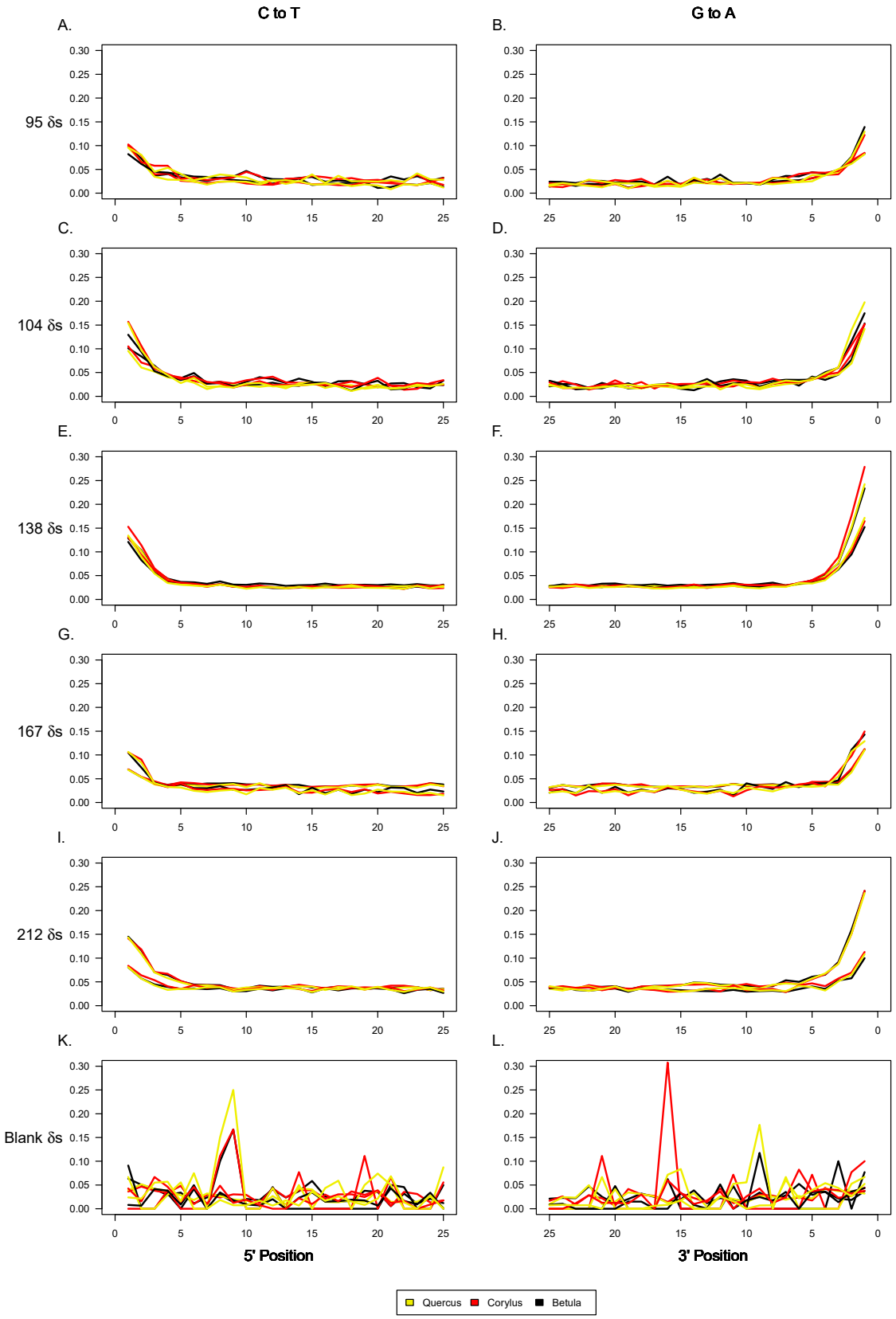

Figure S4.2 C to T mismatch distributions of sedaDNA mapped to genomes.

Quercus, *Corylus* and *Betula* genomes used, calculated in mapDamage 2.0[16]

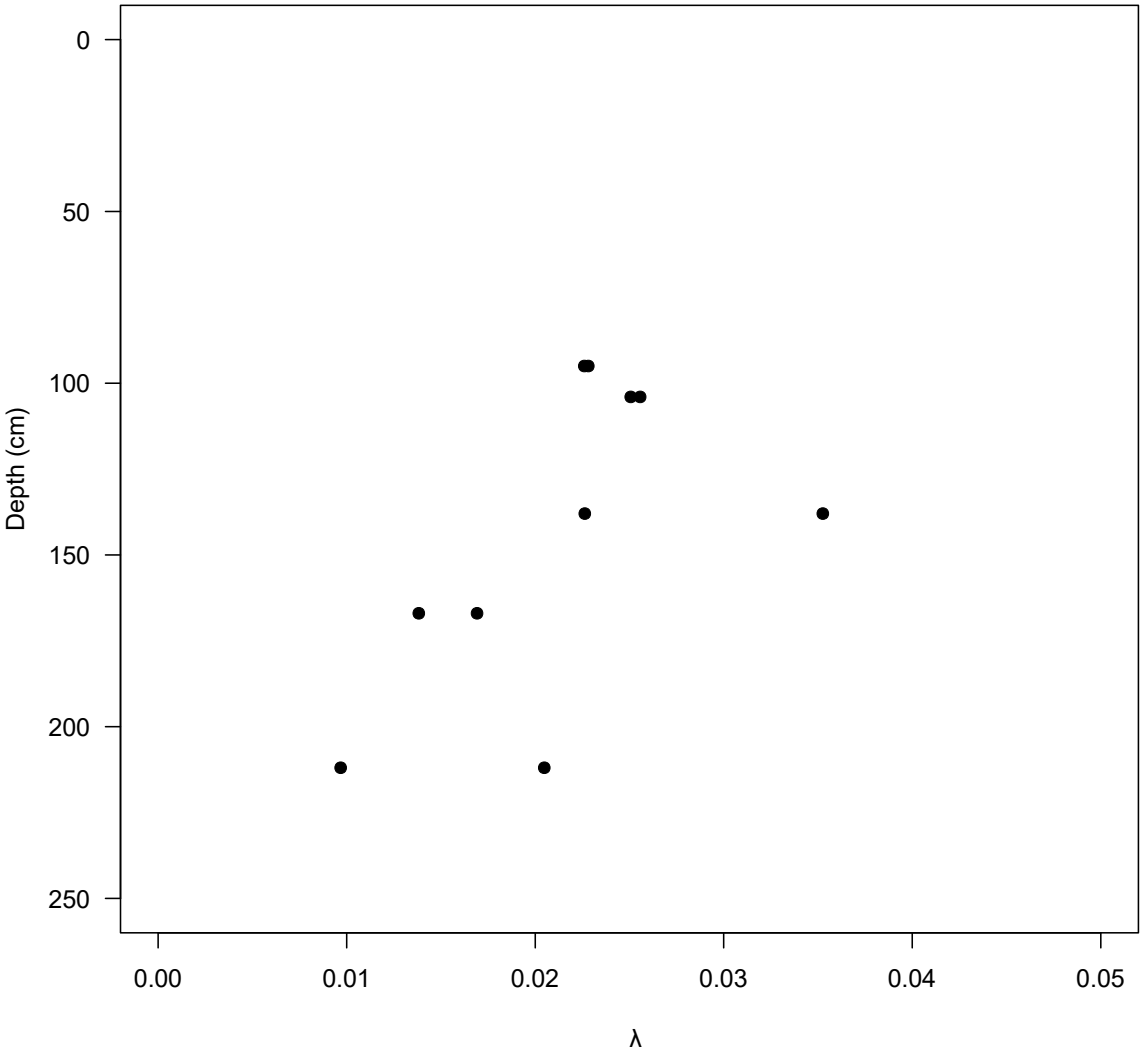

Figure S4.3 DNA fragmentation pattern derived statistics for core ELF001A

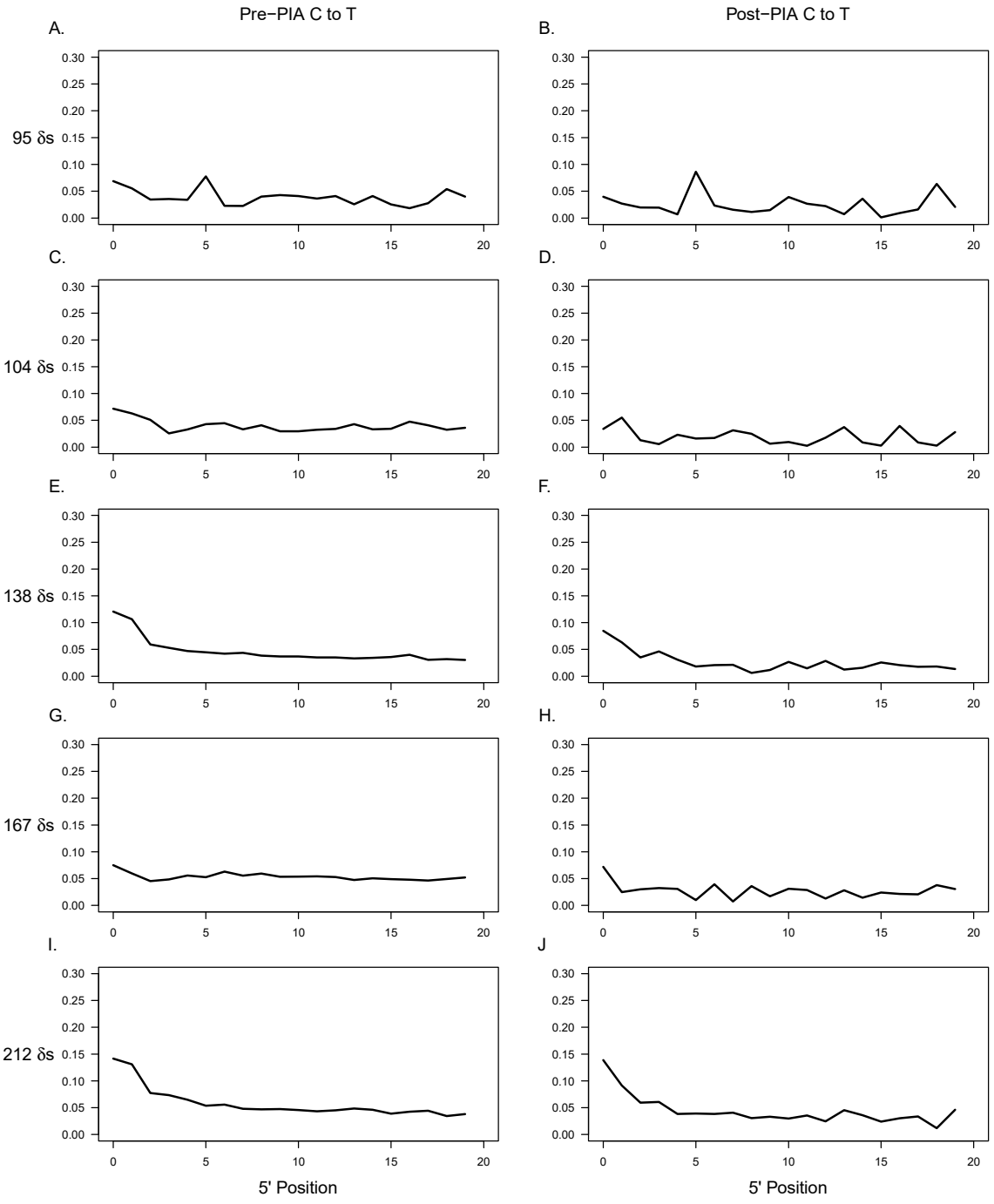

Figure S4.4 Metadamage analysis of C to T transitions across all pre and post PIA filtered sedaDNA

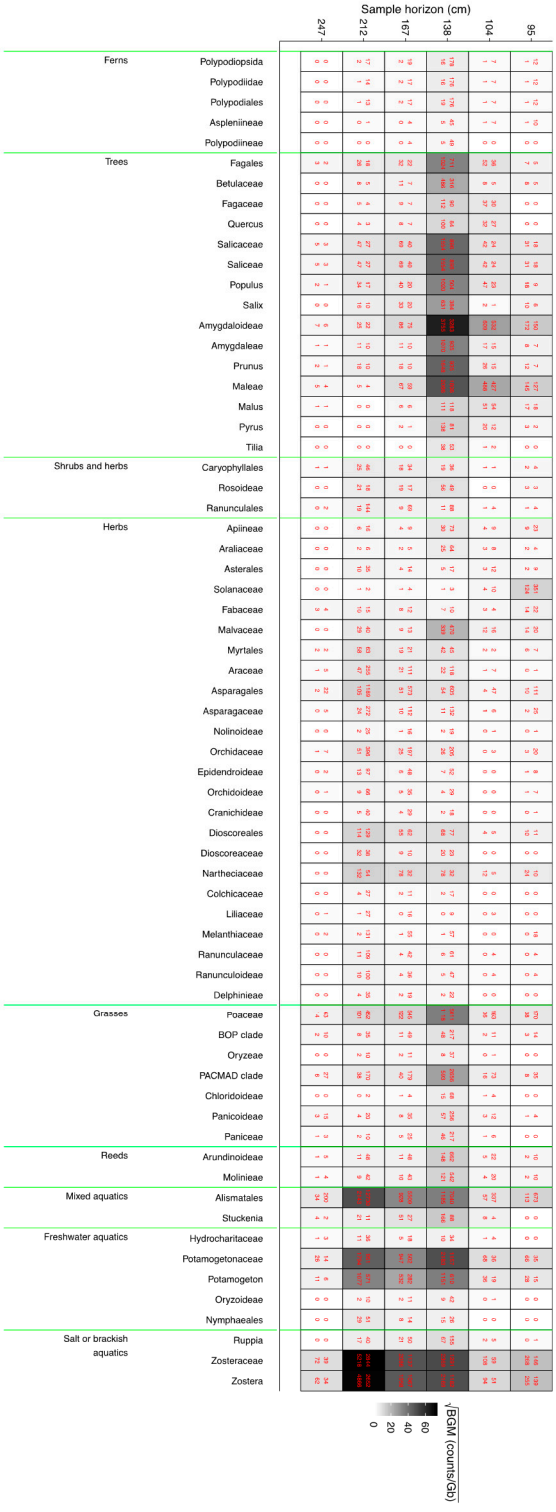

Figure S4.5 ELF001A floral sedaDNA profile.
Numbers above are absolute counts of reads after PIA filtering, numbers below are biogenomic mass (BGM), counts/Gb. Shading represents corresponding BGM values scaled by square root.

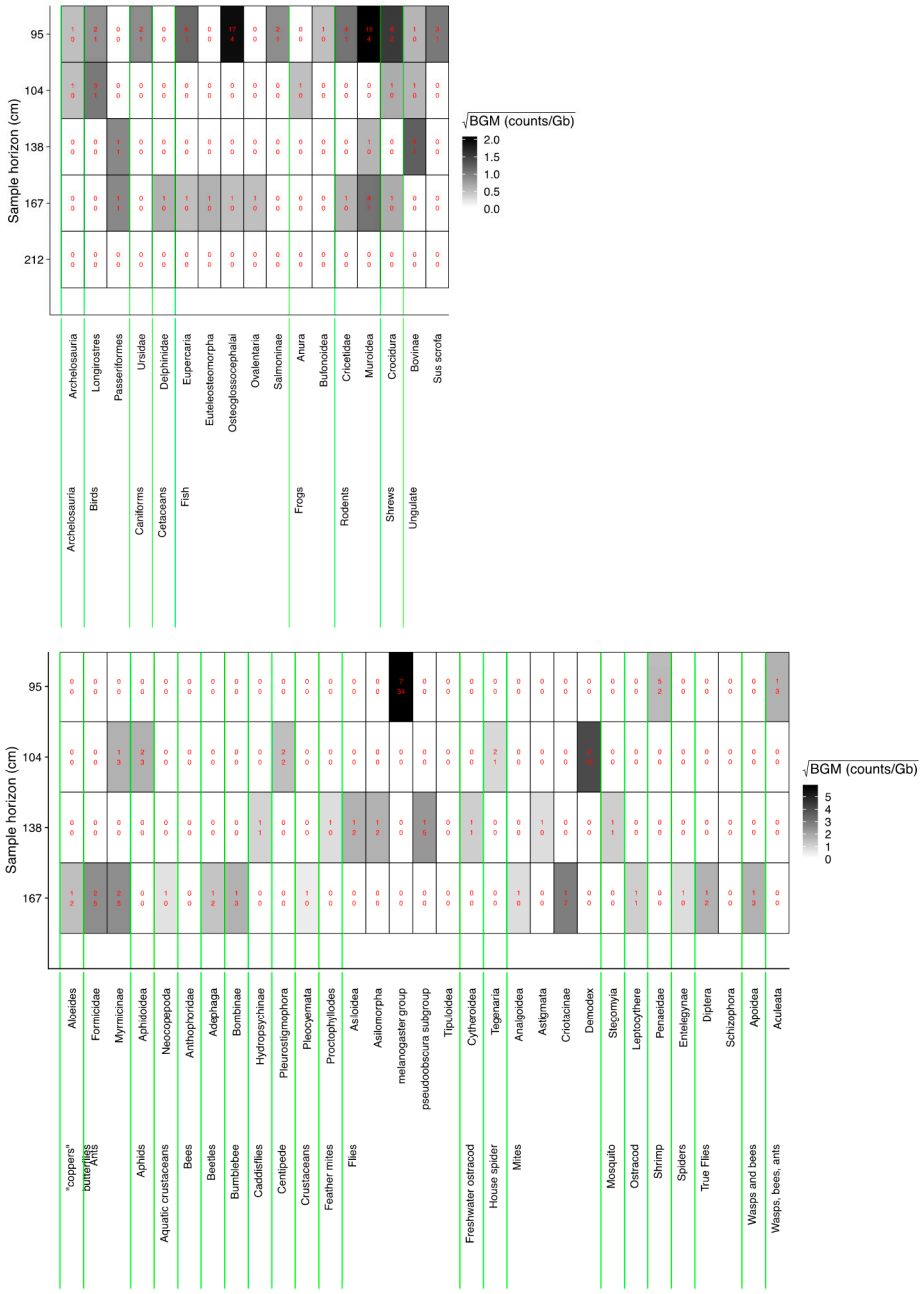

Figure S4.6 ELF001A faunal sedaDNA profile.
Numbers and shading as Figure S4.5. Upper panel: vertebrates, lower panel: invertebrates.

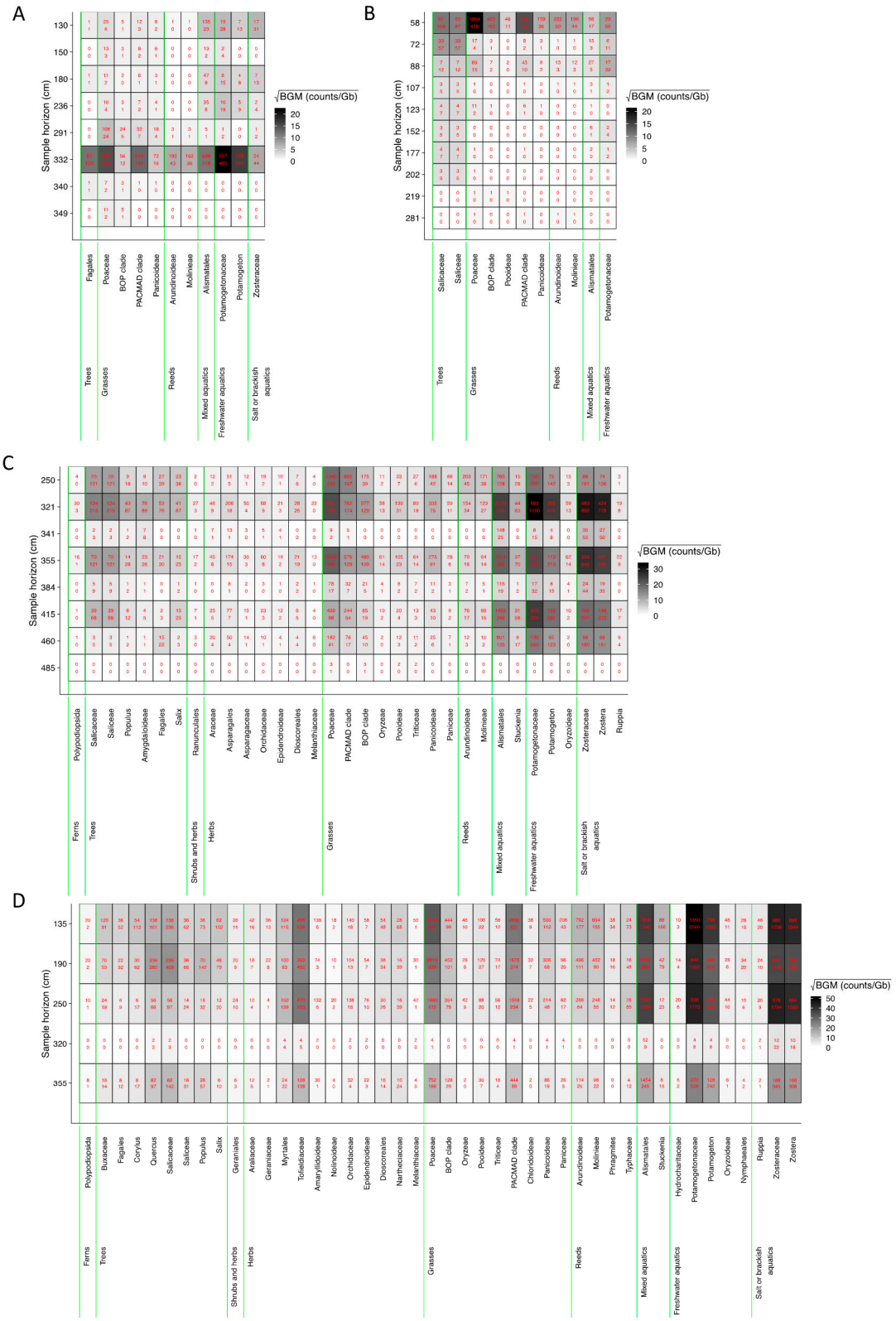

Figure S4.7 Floral sedaDNA profile of other tsunami candidate cores.
Numbers and shading as Figure S4.5. A. ELF003, B. ELF0031A, C. ELF0039, D. ELF0059A.

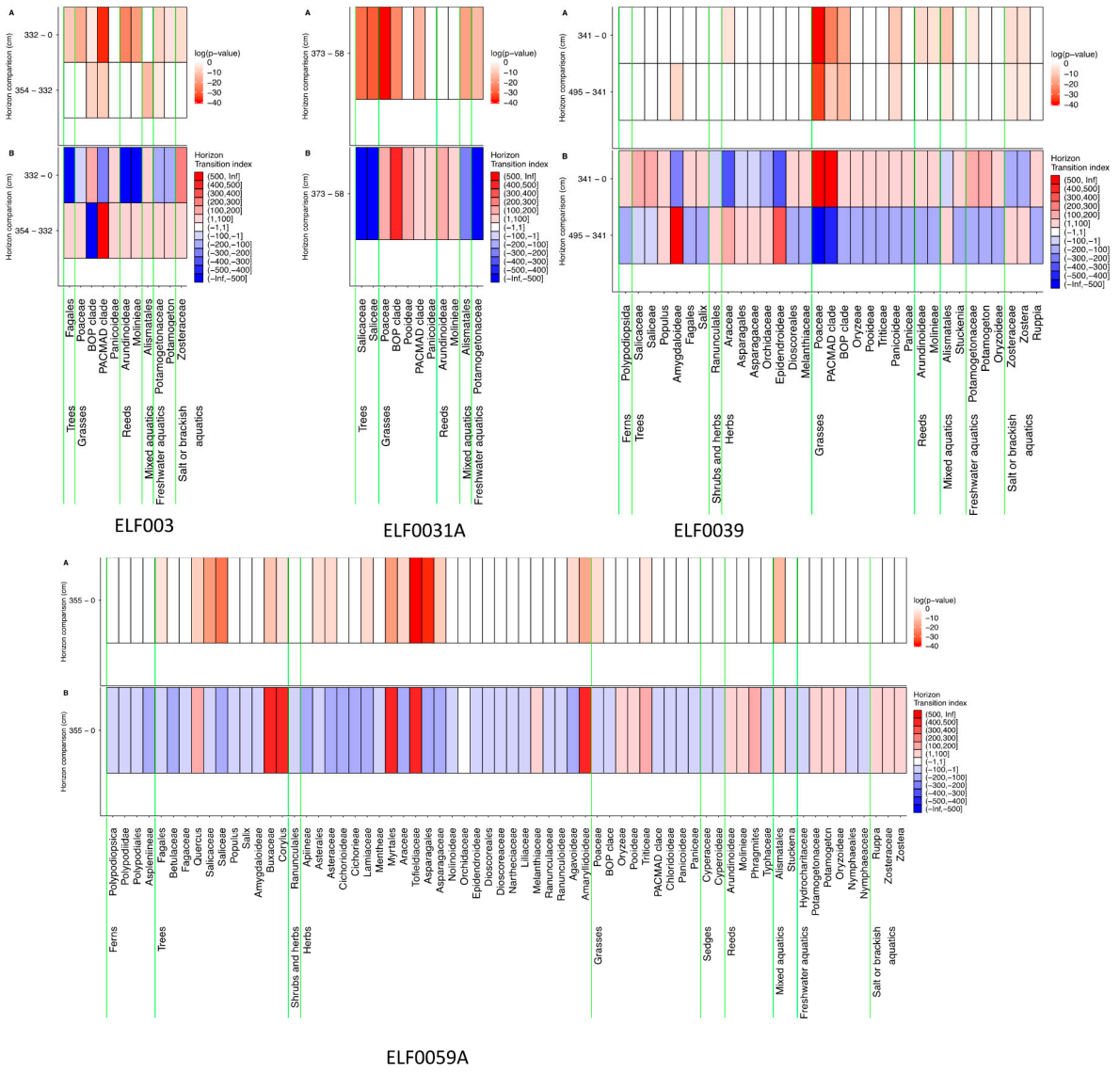

Figure S4.8 sedaDNA change between putative tsunami and adjacent strata
Assessment of taxon change between sample horizons of taxa with abundances > 50 in other tsunami candidate cores identified by seismic survey. Below: Index of change between horizons based on changes in maximum likelihood estimators of the probability taxon being selected from each horizon. Blue indicates a decrease in probability moving up the core, red an increase. Above: Probability of observed taxa counts between pairs of horizons being drawn from the same distribution. A. ELF003, B. ELF0031A, C. ELF0039, D. ELF0059A.

Core	Latitude	Longitude	Elevation (m)	Depth (m)	Sample name	Sequencing platform	Replicate	EMBL unique name
ELF001A	53.321856	1.11754	-21.53	0.95	S81	Illumina MiSeq	1	ELF001A_95_S81_ELFM1D1
ELF001A	53.321856	1.11754	-21.53	0.95	S81	Illumina MiSeq	2	ELF001A_95_S81_ELFM2D2
ELF001A	53.321856	1.11754	-21.53	0.95	S81	Illumina NextSeq	3	ELF001A_95_S81_ELFN1D3
ELF001A	53.321856	1.11754	-21.53	0.95	S81	Illumina NextSeq	4	ELF001A_95_S81_ELFN1D4
ELF001A	53.321856	1.11754	-21.53	1.04	S78	Illumina MiSeq	1	ELF001A_104_S78_ELFM1D1
ELF001A	53.321856	1.11754	-21.53	1.04	S78	Illumina MiSeq	2	ELF001A_104_S78_ELFM2D2
ELF001A	53.321856	1.11754	-21.53	1.04	S78	Illumina NextSeq	3	ELF001A_104_S78_ELFN1D3
ELF001A	53.321856	1.11754	-21.53	1.04	S78	Illumina NextSeq	4	ELF001A_104_S78_ELFN1D4
ELF001A	53.321856	1.11754	-21.53	1.2	D1	Illumina NextSeq	1	ELF001A_120_D1_ELFN3D1
ELF001A	53.321856	1.11754	-21.53	1.2	D2	Illumina NextSeq	2	ELF001A_120_D2_ELFN3D2
ELF001A	53.321856	1.11754	-21.53	1.26	E1	Illumina NextSeq	1	ELF001A_126_E1_ELFN3D1
ELF001A	53.321856	1.11754	-21.53	1.26	E1	Illumina NextSeq	2	ELF001A_126_E2_ELFN3D2
ELF001A	53.321856	1.11754	-21.53	1.38	F1	Illumina NextSeq	1	ELF001A_138_F1_ELFN3D1
ELF001A	53.321856	1.11754	-21.53	1.38	F2	Illumina NextSeq	2	ELF001A_138_F2_ELFN3D2
ELF001A	53.321856	1.11754	-21.53	1.38	S79	Illumina MiSeq	1	ELF001A_138_S79_ELFM1D1
ELF001A	53.321856	1.11754	-21.53	1.38	S79	Illumina MiSeq	2	ELF001A_138_S79_ELFM2D2
ELF001A	53.321856	1.11754	-21.53	1.38	S79	Illumina NextSeq	3	ELF001A_138_S79_ELFN1D3
ELF001A	53.321856	1.11754	-21.53	1.38	S79	Illumina NextSeq	4	ELF001A_138_S79_ELFN1D4
ELF001A	53.321856	1.11754	-21.53	1.49	G1	Illumina NextSeq	1	ELF001A_149_G1_ELFN3D1
ELF001A	53.321856	1.11754	-21.53	1.49	G2	Illumina NextSeq	2	ELF001A_149_G2_ELFN3D2
ELF001A	53.321856	1.11754	-21.53	1.67	S80	Illumina MiSeq	1	ELF001A_167_S80_ELFM1D1
ELF001A	53.321856	1.11754	-21.53	1.67	S80	Illumina MiSeq	2	ELF001A_167_S80_ELFM2D2
ELF001A	53.321856	1.11754	-21.53	1.67	S80	Illumina NextSeq	3	ELF001A_167_S80_ELFN1D3
ELF001A	53.321856	1.11754	-21.53	1.67	S80	Illumina NextSeq	4	ELF001A_167_S80_ELFN1D4
ELF001A	53.321856	1.11754	-21.53	2.12	S75	Illumina MiSeq	1	ELF001A_212_S75_ELFM1D1
ELF001A	53.321856	1.11754	-21.53	2.12	S75	Illumina MiSeq	2	ELF001A_212_S75_ELFM2D2
ELF001A	53.321856	1.11754	-21.53	2.12	S75	Illumina NextSeq	3	ELF001A_212_S75_ELFN1D3
ELF001A	53.321856	1.11754	-21.53	2.12	S75	Illumina NextSeq	4	ELF001A_212_S75_ELFN1D4
ELF001A	53.321856	1.11754	-21.53	2.47	S76	Illumina MiSeq	1	ELF001A_247_S76_ELFM1D1
ELF001A	53.321856	1.11754	-21.53	2.47	S76	Illumina MiSeq	2	ELF001A_247_S76_ELFM2D2
ELF001A	53.321856	1.11754	-21.53	2.82	S77	Illumina MiSeq	1	ELF001A_282_S77_ELFM1D1
ELF001A	53.321856	1.11754	-21.53	2.82	S77	Illumina MiSeq	2	ELF001A_282_S77_ELFM2D2
ELF001A	53.321856	1.11754	-21.53	3.1	S73	Illumina MiSeq	1	ELF001A_310_S73_ELFM1D1
ELF001A	53.321856	1.11754	-21.53	3.1	S73	Illumina MiSeq	2	ELF001A_310_S73_ELFM2D2
ELF001A	53.321856	1.11754	-21.53	3.48	S74	Illumina MiSeq	1	ELF001A_348_S74_ELFM1D1
ELF001A	53.321856	1.11754	-21.53	3.48	S74	Illumina MiSeq	2	ELF001A_348_S74_ELFM2D2
ELF003	53.292367	1.026994	-26.25	1.3	S40	Illumina MiSeq	1	ELF003_130_S40_ELFM1D1
ELF003	53.292367	1.026994	-26.25	1.3	S40	Illumina MiSeq	2	ELF003_130_S40_ELFM2D2
ELF003	53.292367	1.026994	-26.25	1.5	S41	Illumina MiSeq	1	ELF003_150_S41_ELFM1D1
ELF003	53.292367	1.026994	-26.25	1.5	S41	Illumina MiSeq	2	ELF003_150_S41_ELFM2D2
ELF003	53.292367	1.026994	-26.25	1.8	S42	Illumina MiSeq	1	ELF003_180_S42_ELFM1D1
ELF003	53.292367	1.026994	-26.25	1.8	S42	Illumina MiSeq	2	ELF003_180_S42_ELFM2D2
ELF003	53.292367	1.026994	-26.25	2.36	S43	Illumina MiSeq	1	ELF003_236_S43_ELFM1D1
ELF003	53.292367	1.026994	-26.25	2.36	S43	Illumina MiSeq	2	ELF003_236_S43_ELFM2D2
ELF003	53.292367	1.026994	-26.25	2.91	S44	Illumina MiSeq	1	ELF003_291_S44_ELFM1D1
ELF003	53.292367	1.026994	-26.25	2.91	S44	Illumina MiSeq	2	ELF003_291_S44_ELFM2D2
ELF003	53.292367	1.026994	-26.25	3.32	B1	Illumina NextSeq	1	ELF003_332_B1_ELFN3D1
ELF003	53.292367	1.026994	-26.25	3.32	B1	Illumina NextSeq	2	ELF003_332_B2_ELFN3D2
ELF003	53.292367	1.026994	-26.25	3.4	S45	Illumina MiSeq	1	ELF003_340_S45_ELFM1D1
ELF003	53.292367	1.026994	-26.25	3.4	S45	Illumina MiSeq	2	ELF003_340_S45_ELFM2D2
ELF003	53.292367	1.026994	-26.25	3.49	S46	Illumina MiSeq	1	ELF003_349_S46_ELFM1D1
ELF003	53.292367	1.026994	-26.25	3.49	S46	Illumina MiSeq	2	ELF003_349_S46_ELFM2D2
-	52.375306	-1.55206	94	0	S93	Illumina MiSeq	1	Blank_S93_ELFM1D1
-	52.375306	-1.55206	94	0	S94	Illumina MiSeq	1	Blank_S94_ELFM1D1
-	52.375306	-1.55206	94	0	S95	Illumina MiSeq	1	Blank_S95_ELFM1D1
-	52.375306	-1.55206	94	0	S96	Illumina MiSeq	1	Blank_S96_ELFM1D1
-	52.375306	-1.55206	94	0	S97	Illumina MiSeq	1	Blank_S97_ELFM1D1
-	52.375306	-1.55206	94	0	S98	Illumina MiSeq	1	Blank_S98_ELFM1D1
-	52.375306	-1.55206	94	0	S99	Illumina MiSeq	1	Blank_S99_ELFM1D1
-	52.375306	-1.55206	94	0	S100	Illumina MiSeq	1	Blank_S100_ELFM1D1
-	52.375306	-1.55206	94	0	S101	Illumina MiSeq	1	Blank_S101_ELFM1D1
-	52.375306	-1.55206	94	0	S102	Illumina MiSeq	1	Blank_S102_ELFM1D1
-	52.375306	-1.55206	94	0	S103	Illumina MiSeq	1	Blank_S103_ELFM1D1
-	52.375306	-1.55206	94	0	S104	Illumina MiSeq	1	Blank_S104_ELFM1D1
-	52.375306	-1.55206	94	0	S105	Illumina MiSeq	1	Blank_S105_ELFM1D1
-	52.375306	-1.55206	94	0	S106	Illumina MiSeq	1	Blank_S106_ELFM1D1
-	52.375306	-1.55206	94	0	S107	Illumina MiSeq	1	Blank_S107_ELFM1D1
-	52.375306	-1.55206	94	0	S93	Illumina MiSeq	2	Blank_S93_ELFM2D2
-	52.375306	-1.55206	94	0	S94	Illumina MiSeq	2	Blank_S94_ELFM2D2
-	52.375306	-1.55206	94	0	S95	Illumina MiSeq	2	Blank_S95_ELFM2D2
-	52.375306	-1.55206	94	0	S96	Illumina MiSeq	2	Blank_S96_ELFM2D2
-	52.375306	-1.55206	94	0	S97	Illumina MiSeq	2	Blank_S97_ELFM2D2
-	52.375306	-1.55206	94	0	S98	Illumina MiSeq	2	Blank_S98_ELFM2D2
-	52.375306	-1.55206	94	0	S99	Illumina MiSeq	2	Blank_S99_ELFM2D2
-	52.375306	-1.55206	94	0	S100	Illumina MiSeq	2	Blank_S10O_ELFM2D2
-	52.375306	-1.55206	94	0	S101	Illumina MiSeq	2	Blank_S101_ELFM2D2
-	52.375306	-1.55206	94	0	S102	Illumina MiSeq	2	Blank_S102_ELFM2D2
-	52.375306	-1.55206	94	0	S103	Illumina MiSeq	2	Blank_S103_ELFM2D2
-	52.375306	-1.55206	94	0	S104	Illumina MiSeq	2	Blank_S104_ELFM2D2
-	52.375306	-1.55206	94	0	S105	Illumina MiSeq	2	Blank_S105_ELFM2D2
-	52.375306	-1.55206	94	0	S106	Illumina MiSeq	2	Blank_S106_ELFM2D2
-	52.375306	-1.55206	94	0	S107	Illumina MiSeq	2	Blank_S107_ELFM2D2
-	52.375306	-1.55206	94	0	S108	Illumina MiSeq	2	Blank_S108_ELFM2D1
-	52.375306	-1.55206	94	0	S13	Illumina NextSeq	1	Blank_S13_ELFN1D1
-	52.375306	-1.55206	94	0	S6	Illumina NextSeq	1	Blank_B6M2_S6_ELFN1D1
-	52.375306	-1.55206	94	0	S7	Illumina NextSeq	1	Blank_B7M2_B14M1_S7_ELFN1D1
ELF031A	53.1312833	1.35302958	-28	0.58	C1	Illumina NextSeq	1	ELF031A_58_C1_ELFN3D1
ELF031A	53.1312833	1.35302958	-28	0.58	C2	Illumina NextSeq	2	ELF031A_58_C2_ELFN3D2
ELF031A	53.1312833	1.35302958	-28	0.72	31	Illumina NextSeq	1	ELF031A_72_31_ELFN2D1
ELF031A	53.1312833	1.35302958	-28	0.88	32	Illumina NextSeq	1	ELF031A_88_32_ELFN2D1
ELF031A	53.1312833	1.35302958	-28	1.07	33	Illumina NextSeq	1	ELF031A_107_33_ELFN2D1
ELF031A	53.1312833	1.35302958	-28	1.23	34	Illumina NextSeq	1	ELF031A_123_34_ELFN2D1
ELF031A	53.1312833	1.35302958	-28	1.52	35	Illumina NextSeq	1	ELF031A_152_35_ELFN2D1
ELF031A	53.1312833	1.35302958	-28	1.77	36	Illumina NextSeq	1	ELF031A_177_36_ELFN2D1
ELF031A	53.1312833	1.35302958	-28	2.02	37	Illumina NextSeq	1	ELF031A_202_37_ELFN2D1
ELF031A	53.1312833	1.35302958	-28	2.19	38	Illumina NextSeq	1	ELF031A_219_38_ELFN2D1
ELF031A	53.1312833	1.35302958	-28	2.81	39	Illumina NextSeq	1	ELF031A_281_39_ELFN2D1
ELF031A	53.1312833	1.35302958	-28	2.81	40	Illumina NextSeq	1	ELF031A_310_40_ELFN2D1
ELF039	53.2129222	1.20542119	-38.3	1.45	59	Illumina NextSeq	1	ELF039_145_59_ELFN2D1
ELF039	53.2129222	1.20542119	-38.3	2.5	60	Illumina NextSeq	1	ELF039_250_60_ELFN2D1
ELF039	53.2129222	1.20542119	-38.3	3.21	61	Illumina NextSeq	1	ELF039_321_61_ELFN2D1
ELF039	53.2129222	1.20542119	-38.3	3.41	A1	Illumina NextSeq	1	ELF039_341_A1_ELFN3_D1
ELF039	53.2129222	1.20542119	-38.3	3.41	A2	Illumina NextSeq	2	ELF039_341_A2_ELFN3_D2
ELF039	53.2129222	1.20542119	-38.3	3.55	62	Illumina NextSeq	1	ELF039_355_62_ELFN2D1
ELF039	53.2129222	1.20542119	-38.3	3.84	63	Illumina NextSeq	1	ELF039_384_63_ELFN2D1
ELF039	53.2129222	1.20542119	-38.3	4.15	64	Illumina NextSeq	1	ELF039_415_64_ELFN2D1
ELF039	53.2129222	1.20542119	-38.3	4.6	65	Illumina NextSeq	1	ELF039_460_65_ELFN2D1
ELF039	53.2129222	1.20542119	-38.3	4.85	66	Illumina NextSeq	1	ELF039_485_66_ELFN2D1
ELF059A	53.3513054	0.99086431	-22	1.35	115	Illumina NextSeq	1	ELF059A_135_115_ELFN2D1
ELF059A	53.3513054	0.99086431	-22	1.9	116	Illumina NextSeq	1	ELF059A_190_116_ELFN2D1
ELF059A	53.3513054	0.99086431	-22	2.5	117	Illumina NextSeq	1	ELF059A_250_117_ELFN2D1
ELF059A	53.3513054	0.99086431	-22	3.2	118	Illumina NextSeq	1	ELF059A_320_118_ELFN2D1
ELF059A	53.3513054	0.99086431	-22	3.55	119	Illumina NextSeq	1	ELF059A_355_119_ELFN2D1
ELF059A	53.3513054	0.99086431	-22	3.55	119A	Illumina NextSeq	3	ELF059A_355_119A_ELFN3D3
ELF059A	53.3513054	0.99086431	-22	3.55	119B	Illumina NextSeq	4	ELF059A_355_119B_ELFN3D4
-	52.375306	-1.55206	94	0	Blank_B1	Illumina NextSeq	1	Blank_B1_ELFN2D1
-	52.375306	-1.55206	94	0	Blank_B2	Illumina NextSeq	1	Blank_B2_ELFN2D1
-	52.375306	-1.55206	94	0	Blank_B3	Illumina NextSeq	1	Blank_B3_ELFN2D1
-	52.375306	-1.55206	94	0	Blank_B4	Illumina NextSeq	1	Blank_B4_ELFN2D1
-	52.375306	-1.55206	94	0	Blank_B5	Illumina NextSeq	1	Blank_B5_ELFN2D1
-	52.375306	-1.55206	94	0	Blank_B6	Illumina NextSeq	1	Blank_B6_ELFN2D1
-	52.375306	-1.55206	94	0	Blank_B7	Illumina NextSeq	1	Blank_B7_ELFN2D1
-	52.375306	-1.55206	94	0	Blank_B8	Illumina NextSeq	1	Blank_B8_ELFN2D1
-	52.375306	-1.55206	94	0	Blank_B10	Illumina NextSeq	1	Blank_B10_ELFN2D1
-	52.375306	-1.55206	94	0	Blank_B11	Illumina NextSeq	1	Blank_B11_ELFN2D1
-	52.375306	-1.55206	94	0	Blank_B12	Illumina NextSeq	1	Blank_B12_ELFN2D1
-	52.375306	-1.55206	94	0	Blank_B13	Illumina NextSeq	1	Blank_B13_ELFN2D1
-	52.375306	-1.55206	94	0	Blank_B14	Illumina NextSeq	1	Blank_B14_ELFN2D1
-	52.375306	-1.55206	94	0	Blank_B15	Illumina NextSeq	1	Blank_B15_ELFN2D1
-	52.375306	-1.55206	94	0	Blank_B16	Illumina NextSeq	1	Blank_B16_ELFN2D1
-	52.375306	-1.55206	94	0	Blank_B17	Illumina NextSeq	1	Blank_B17_ELFN2D1
-	52.375306	-1.55206	94	0	Blank_B18	Illumina NextSeq	1	Blank_B18_ELFN2D1
-	52.375306	-1.55206	94	0	Blank_B19	Illumina NextSeq	1	Blank_B19_ELFN2D1
-	52.375306	-1.55206	94	0	Blank_B20	Illumina NextSeq	1	Blank_B20_ELFN2D1
-	52.375306	-1.55206	94	0	Blank_B21	Illumina NextSeq	1	Blank_B21_ELFN2D1
-	52.375306	-1.55206	94	0	Blank_B18	Illumina NextSeq	3	Blank_B18_ELFN3D3
-	52.375306	-1.55206	94	0	Blank_R18	Illumina NextSeq	4	Blank_R18_ELFN3D4
-	52.375306	-1.55206	94	0	Blank_X1	Illumina NextSeq	1	Blank_X1_ELFN3_D1
-	52.375306	-1.55206	94	0	Blank_X2	Illumina NextSeq	2	Blank_X2_ELFN3_D2

Table S4.2 SedaDNA sample and read details

Jones, A.P., Tucker, M.E. and Hart, J.K (eds.) 1999 The description and analysis of Quaternary stratigraphic field sections. Quaternary Research Association Technical Guide No. 7. Quaternary Research Association: London. 286pp.

21. Stephenson, A. (1993) Three axis alternating-field demagnetization of rocks and the identification of NRM, GRM, and anistropy. *Journal of Geophysical Research - Atmospheres* 98 (B1), 373 - 381.

22. Hounslow, M. W. (2018) *GM4Edit - a program for managing magnetometer data v5.3*.

23. Dekkers, M. J. (2007) Magnetic Proxy Parameters. In Gubbins, D. and Herrero-Bervera, E. (editors) *Encyclopedia of Geomagnetism and Palaeomagnetism.* Dordrecht, Netherlands: Springer. 525 - 534.

24. Hayashida, A., Nakano, R., Nagashima, A., Seto, K., Yamada, K. and Yonenobu, H. (2015) Magnetic properties of surficial sediments in Lake Ogawara on the Pacific coast of northeastern Japan: spatial variability and correlation with brackish water stratification. *Earth, Planets and Space* 67 (1), 171.

25. Su, Y., Gao, X., Liu, Q., Wang, J., Haberzettl, T., Zhu, L., Li, J., Duan, Z. and Tian, L. (2013) Mineral magnetic study of lacustrine sediments from Lake Pumoyum Co, southern Tibet, over the last 19ka and paleoenvironmental significance. *Tectonophysics* 588, 209-221.

26. Walden, J. (1999) Remanence Measurements. In Walden, J., Oldfield, F., and Smith, J. P. (editors) *Environmental Magnetism: a practical guide.*Technical Guide No. 6. London: Quaternary Research Association. 63 - 88.

27. Gurney, S. D. and White, K. (2005) Sediment magnetic properties of glacial till deposited since the Little Ice Age maximum for selected glaciers at Svartisen and Okstindan, northern Norway. *Boreas* 34 (1), 75-83.

28. Chagué-Goff, C., Szczuciński, W., Shinozaki, T. 2017 Applications of geochemistry in tsunami research: A review, *Earth-Science Reviews*, **165**, (203-244), (2017)

29. Croudace, I., Rindby, A., Rothwell, R., 2006. ITRAX: description and evaluation of a new multi-function X-ray core scanner. In: Rothwell, R. (Ed.), New Techniques in Sediment Core Analysis. Geological Society, London, pp. 51–63

30. Davies, S.J., Lamb, H.F., Roberts, S.J., 2015. Micro-XRF core scanning in palaeolimnology: recent developments. In: Croudace, I.W., Rothwell, R.G. (Eds.), Micro-XRF Studies of Sediment Cores. Springer, Netherlands, pp. 189–226.

31. Marty, J.-C. and Saliot, A. (1982) Aerosols in equatorial Atlantic air: n-alkanes as a function of particle size. *Nature* 298 (5870), 144.

32. Sikes, E. L., Uhle, M. E., Nodder, S. D. and Howard, M. E. (2009) Sources of organic matter in a coastal marine environment: Evidence from n-alkanes and their δ13C distributions in the Hauraki Gulf, New Zealand. *Marine Chemistry* 113 (3-4), 149-163.

33. El Nemr, A., Moneer, A. A., Ragab, S. and El Sikaily, A. (2016) Distribution and sources of n-alkanes and polycyclic aromatic hydrocarbons in shellfish of the Egyptian Red Sea coast. *The Egyptian Journal of Aquatic Research* 42 (2), 121-131.

34. Mille, G., Asia, L., Guiliano, M., Malleret, L. and Doumenq, P. (2007) Hydrocarbons in coastal sediments from the Mediterranean sea (Gulf of Fos area, France). *Marine pollution bulletin* 54 (5), 566-575.

35. Kinnaird, T. C., Dawson, T., Sanderson, D. C. W., Hamilton, D., Cresswell, A. and Rennel, R., 2017. Chronostratigraphy of an eroding complex Atlantic round house, Baile Sear, Scotland. *Journal of Coastal and Island Archaeology*, 14:1, 46-60.

36. Sanderson, D.C.W. and Murphy, S., 2010. Using simple portable OSL measurements and laboratory characterisation to help understand complex and heterogeneous sediment sequences for luminescence dating. *Quaternary Geochronology*, **5** (2), p. 299-305.

37. Burbidge, C.I., Sanderson, D.C.W., Housley, R.A. and Jones, P.A., 2007. Survey of palaeolithic sites by luminescence profiling, a case study form Eastern Europe. *Quaternary Geochronology*, **2**, p. 296–302.

38. Sanderson, D.C.W., Bishop, P., Stark, M.T. and Spencer, J.Q., 2003. Luminescence dating of anthropogenically reset canal sediments from Angkor Borei, Mekong Delta, Cambodia. *Quaternary Science Reviews*, **22**, p. 1111-1121.

39. Murray, A. S. and Wintle, A. G., 2000. Luminescence dating of quartz using an improved single-aliquot regenerative-dose protocol. *Radiation Measurements*, **32**(1), p. 57-73.

40. Guérin, G., Christophe, C., Philippe, A., Murray, A. S., Thomsen, K. J., Tribolo, C., Urbanova, P., Jain, M., Guibert, P., Mercier, N., Kreutzer, S., and Lahaye, C., 2017. Absorbed dose, equivalent dose, measured dose rates, and implications for OSL age estimates: Introducing the Average Dose Model: *Quaternary Geochronology*, **41**, p. 163-173.

41. Zhang, W., Hu, Z., Liu, Y., Chen, H., Gao, S., and Gaschnig, R. M., 2012, Total Rock Dissolution Using Ammonium Bifluoride (NH4HF2) in Screw-Top Teflon Vials: A New Development in Open-Vessel Digestion: Analytical Chemistry, v. 84, no. 24, p. 10686-10693.

42. Guérin, G., Mercier, N. and Adamiec, G., 2011. Dose-rate conversion factors: update. *Ancient TL*, **29**, p. 5-8.

43. Mejdahl, V., 1979. Thermoluminescence dating: Beta-dose attenuation in quartz grains. *Archeometry*, **29**(1), p. 61-72.

44. Bondevik, S., S.K. Stormo & G. Skjerdal. 2012. Green mosses date the Storegga tsunami to the chilliest decades of the 8.2ka cold event. *Quaternary Science Reviews* 45: 1–6.

45. Bondevik, S. 2019. Tsunami from the Storegga Landslide. In R.A. Meyers (ed.) *Encyclopedia of Complexity and Systems Science*. Berlin: Springer.

46. Dawson, A., Bondevik, S., & Teller, J. T. (2011). Relative timing of the Storegga submarine slide, methane release, and climate change during the 8.2 ka cold event. *The Holocene*, *21*(7), 1167–1171.

47. Dietze, M., Kreutzer, S., Fuchs, M. C., Burow, C., Fischer, M. and Schmidt, C., 2013. A practical guide to the R package Luminescence. *Ancient TL*, **32**, p. 11-18.

48. Stuiver, M., Kra, R.S., 1986. Editorial comment, Radiocarbon 28, ii.

49. Stuiver, M., Polach, H.A., 1977. Reporting of ^{14}C data, Radiocarbon 19, 355–363.

50. Bronk Ramsey, C., 2009. Bayesian analysis of radiocarbon dates, Radiocarbon 51, 337–360.

51. Reimer, P.J., Bard, E., Bayliss, A., Beck, J.W., Blackwell, P.G., Bronk Ramsey, C., Buck, C.E., Cheng, H., Edwards, R.L., Friedrich, M., Grootes, P.M., Guilderson, T.P., Haflidason, H., Hajdas, I., Hatté, C., Heaton, T.J., Hoffmann, D.L., Hogg, A.G., Hughen, K.A., Kaiser, K.F., Kromer, B., Manning, S.W., Niu, M., Reimer, R.W., Richards, D.A., Scott, E.M., Southon, J.R., Staff, R.A., Turney, C.S.M., van der Plicht, J., 2013. IntCal13 and Marine13 radiocarbon age calibration curves 0–50,000 years cal BP, Radiocarbon 55, 1869–1887.

52. Moore, P. D., Webb, J. & Collinson, M. 1991. *Pollen analysis*, 2nd Edition. Blackwell Scientific, Oxford.

53. Bennett, K. D., Whittington, G. & Edwards, K. J. 1994. Recent plant nomenclature changes and pollen morphology in the British Isles. *Quaternary Newsletter*, **73**, p.1-6.

54. Grimm, E. C. 2004. Tilia and TGView. Springfield, Illinois, Illinois State Museum.

55. Plater, A.J., Horton, B.P., Haworth, E.Y., Appleby, P.G., Zong, Y., Wright, M.R. & Rutherford, M.M. (2000). Holocene tidal levels and sedimentation using a diatom-based palaeoenvironmental reconstruction: the Tees estuary, northeastern England. *The Holocene*, 10 (4), 441-452.

56. van Der Werff & Huls (1958-1974). Diatomeeënflora van Nederland. Eight parts, published privately by van der Werff, De Hoef (U), The Netherlands.

57. Hendy, N.I. (1964). An introductory account of the smaller algae of the British coastal waters. Part V: Bacillariophyceae (Diatoms). Fisheries Investigation Series, I, H.M.S.O., London.

58. Krammer, K. & Lange-Bertalot, H. (1986-1991). Subwasserflora von Mitteleuropa. Bacciliarophyceae: 2 (1) Naviculaceae; 2 (2) Bacillariacceae, Epithemiaceae, Surirellaceae; 2 (3) Centrales, Fragilariaceae, Eunotiaceae; 2 (4) Achnanthaceae. Fischer, Stuttgart.

59. Vos, P.C. & de Wolf, H. (1988). Methodological aspects of palaeo-ecological diatom research in coastal areas of the Netherlands. Geologie en Mijnbouw, 67, 31-40.

60. Vos, P.C. & de Wolf, H. (1993). Diatoms as a tool for reconstructing sedimentary environments in coastal wetlands: methodological aspects. Hydrobiologia, 269/270, 285-96.

61. Van Dam, H., Mertens, A. & Seinkeldam, J. (1994). A coded checklist and ecological indicator values of freshwater diatoms from the Netherlands. Netherlands Journal of Aquatic Ecology, 28, (1), 117-133.

62. Denys, L. (1991-92). A check-list of the diatoms in the Holocene deposits of the western Belgian coastal plain with a survey of their apparent ecological requirements: I. Introduction, ecological code and complete list. Service Geologique de Belgique, professional paper 246.

63. Denys, L. (1994). Diatom assemblages along a former intertidal gradient: a palaeoecological study of a subboreal clay layer (western coastal plain, Belgium). Netherlands Journal of Aquatic Ecology. 28, 1, 85-96.

64. Edsbagge, H. (1966)The composition of the epiphytic diatom flora on the Swedish West Coast, Botanica marina, 11, 68-71.

65. Werner, D. (1974). The Biology of Diatoms. University of California Press, 498pp.

66. Aleem, A.A. (1950) Distribution and ecology of British marine littoral diatoms. Journal of Ecology, 38, 75-106.

67. Tanaka, N. (1986) Adhesive Strength of Epiphytic Diatoms on Various Seaweeds. Bulletin of the Japanese Society of Scientific Fisheries 52 (5), 817-821

68. WORMS EDITORIAL TEAM**,** 2018. 'World Register of Marine Species'. Available at: http: / /ww-w.marinespecies.org/

69. Graham, A., 1971. *British Prosobranchs.* London: Academic Press/ The Linnean Society

70. Allcock, A.L. Er AL., 2017. Molluscs (Phylum Mollusca). In *Handbook of the Marine Fauna of North-West Europe.* Oxford: Oxford University Press, pp. 455-602.

71. Donato, S.V., et al., 2008. 'Identifying tsunami deposits using bivalve shell taphonomy'. *Geology,* **36,** pp .199-202.

72. Gilbert, M. T. P., Bandelt, H. J., Hofreiter, M. & Barnes, I. 2005. Assessing ancient DNA studies. *Trends in Ecology & Evolution,* 20**,** 541-544.

73. Meyer, M. & Kircher, M. 2010. Illumina sequencing library preparation for highly multiplexed target capture and sequencing. *Cold Spring Harbor Protocols,* 2010**,** pdb. prot5448.

74. Kircher, M., Sawyer, S. & Meyer, M. 2012. Double indexing overcomes inaccuracies in multiplex sequencing on the Illumina platform. *Nucleic Acids Research,* 40**,** e3-e3.

75. Rohland, N. & Reich, D. 2012. Cost-effective, high-throughput DNA sequencing libraries for multiplexed target capture. *Genome Research,* 22**,** 939-946.

76. Lindgreen, S. 2012. AdapterRemoval: easy cleaning of next-generation sequencing reads. *BMC Research Notes,* 5**,** 337.

77. Andrews, S. 2010. FastQC: A quality control tool for high throughput sequence data. Available online at: http://www.bioinformatics.babraham.ac.uk/projects/fastqc

78. Gordon, A. & Hannon, G. 2010. Fastx-toolkit. FASTQ/A short-reads pre-processing tools. *Unpublished Available online at: http://hannonlab. cshl. edu/fastx_toolkit*.

79. Zhang Z., Schwartz S., Wagner L., & Miller W. (2000), "A greedy algorithm for aligning DNA sequences" J Comput Biol 2000; 7(1-2):203-14.

80. Huson, D. H., Mitra, S., Ruscheweyh, H.-J., Weber, N. & Schuster, S. C. 2011. Integrative analysis of environmental sequences using MEGAN4. *Genome Research,* 21**,** 1552-1560.

81. Smith et al. Sedimentary DNA from a submerged site reveals wheat in the British Isles 8,000 years ago. *Science* 347:998-1001. (2015)

82. Li, H. & Durbin, R. 2009. Fast and accurate short read alignment with Burrows–Wheeler transform. *Bioinformatics,* 25**,** 1754-1760.

83. Li, H., Handsaker, B., Wysoker, A., Fennell, T., Ruan, J., Homer, N., Marth, G., Abecasis, G. & Durbin, R. 2009. The sequence alignment/map format and SAMtools. *Bioinformatics,* 25**,** 2078-2079.

84. Depristo, M. A., Banks, E., Poplin, R., Garimella, K. V., Maguire, J. R., Hartl, C., Philippakis, A. A., Del Angel, G., Rivas, M. A. & Hanna, M. 2011. A framework for variation discovery and genotyping using next-generation DNA sequencing data. *Nature Genetics,* 43**,** 491.

85. Needleman, Saul B. & Wunsch, Christian D. (1970). "A general method applicable to the search for similarities in the amino acid sequence of two proteins". *Journal of Molecular Biology*. **48** (3): 443–53.

86. Wagner et al. High throughput DNA sequencing of ancient wood. *Mol. Ecol.* 27:1138–1154 (2018)

87. Lindahl, T. and Nyberg, B. (1972) Rate of depurination of native deoxyribonucleic acid. *Biochemistry*, **11**, 3610-3618.

88. Greer, S. and Zamenhof, S. (1962) Studies on depurination of DNA by heat. *Journal of Molecular Biology*, **4**, 123-141.

89. Corinaldesi, C., Beolchini, F. and Dell'Anno, A. (2008) Damage and degradation rates of extracellular DNA in marine sediments: implications for the preservation of gene sequences. *Molecular Ecology*, **17**, 3939-3951.

90. Corinaldesi, C., Barucca, M., Luna, G. and Dell'Anno, A. (2011) Preservation, origin and genetic imprint of extracellular DNA in permanently anoxic deep-sea sediments. *Molecular Ecology*, **20**, 642-654.

91. Haile J et al. Ancient DNA Chronology within Sediment Deposits: Are Paleobiological Reconstructions Possible and Is DNA Leaching a Factor? *Mol. Biol. Evol.* 24:982-989. (2007)